UNIVERSITY OF OKLAHOMA

GRADUATE COLLEGE

VERIFICATION OF 10-METER WIND FORECASTS FROM NSSL-WRF IN PREDICTING SEVERE WIND-PRODUCING MCSS

A THESIS

SUBMITTED TO THE GRADUATE FACULTY

in partial fulfillment of the requirements for the

Degree of

MASTER OF SCIENCE IN METEOROLOGY

By

JEFFREY MARK MILNE
Norman, Oklahoma
2016

VERIFICATION OF 10-METER WIND FORECASTS FROM NSSL-WRF IN PREDICTING SEVERE WIND-PRODUCING MCSS

A THESIS APPROVED FOR THE
SCHOOL OF METEOROLOGY

BY

Dr. Steven Cavallo, chair

Dr. Harold Brooks, co-chair

Dr. Adam Clark

Dr. Evgeni Fedorovich

Acknowledgments

I would like to thank Dr. Israel Jirak of the Storm Prediction Center and Robert Hepper of the Cooperative Institute for Mesoscale Meteorological Studies for their assistance and guidance with this project. I would also like to thank Dr. Harold Brooks for advising me. Additionally, I would like to thank my committee members, Dr. Steven Cavallo, Dr. Adam Clark, and Dr. Evgeni Fedorovich.

Model Evaluation Tools (MET) was developed at the National Center for Atmospheric Research (NCAR) through grants from the United States Air Force Weather Agency (AFWA) and the National Oceanic and Atmospheric Administration (NOAA). NCAR is sponsored by the United States National Science Foundation.

Table of Contents

List of Tables

List of Figures

Abstract

Predicting convective winds associated with mesoscale convective systems (MCSs) remains a major challenge for operational severe weather forecasters. To assess the performance of the Weather Research and Forecasting Model run by the National Severe Storms Laboratory (NSSL-WRF) in forecasting severe wind-producing MCSs between 2012 and 2014, a climatology of these MCSs was developed. Severe wind-producing MCSs were first manually identified by finding swaths of severe wind reports caused by MCSs through inspection of radar reflectivity structure to ensure organized convective mode. To objectively identify severe wind-producing MCSs using an object-based approach, storm reports were filtered based on nearby radar reflectivity. A variety of subsets of severe wind reports were also used. Reports were converted to spatial probabilities via Gaussian smoothing so that objects could be identified. Objects were identified using the Method for Object-based Diagnostic Evaluation (MODE) by testing various minimum intensity and area thresholds to determine which thresholds most accurately matched the manually identified severe wind-producing MCSs. Objects identified based on radar-filtered storm reports most accurately matched manually identified severe wind-producing MCSs. This allowed for development of an object-based climatology of severe wind-producing MCSs. This climatology shows a maximum of severe wind-producing MCSs near the Ohio River Valley with another relative maximum on the Georgia-Alabama border. All identified severe wind-producing MCSs occurred east of the Rocky Mountains. Severe wind-producing MCSs occurred most often in June and least often in November.

Daily maximum 10 m wind forecasts for the 24 hours beginning at 12Z (i.e., f12-f36) were generated from 0000 UTC NSSL-WRF hourly maximum 10 m wind fields. The same smoothing and radar filtering (with simulated reflectivity) that was applied to storm reports was also applied to various forecast daily maximum 10 m wind thresholds between 15 kt and 60 kt. The same intensity and size thresholds were applied to both forecast and observation fields in identifying objects. Forecasts were then verified both on a grid-point-by-grid-point basis, on a grid-based basis using MODE, and on an object-matching basis using MODE. Object-matching utilizes a fuzzy logic algorithm to match forecast and observed objects. Grid-point verification yielded no useful results, with a high number of false alarms dominating any signal. Across a range of wind speed thresholds, the 10 m wind field has a critical success index of around 0.07 when using grid-based verification using MODE and around 0.15 when using MODE object-based verification. Lower wind speed thresholds over-forecast severe wind-producing MCSs and approach a probability of detection (POD) near 100% for very low wind speed thresholds. As wind speed thresholds increase, the POD decreases sharply without much improvement in the false alarm ratio (FAR). For very high wind speed thresholds, very few events are forecast, so both POD and FAR are low. Though the lower thresholds have slightly lower CSIs than higher thresholds, the large increase in POD with a small penalty in FAR suggests that the lower thresholds may be of more utility to forecasters.

Chapter 1

Introduction and Background

1.1 Motivation

Severe wind reports account for approximately half of all severe storm reports received between 2012-14, and Brooks (2013) suggests that severe wind events will increase as the Earth's climate changes. However, forecasting for severe convective wind is a challenge for forecasters. As convection-allowing models (CAMs) have become more prevalent, forecasters can see explicit model forecasts of thunderstorms. Though CAMs can provide information about convective mode (i.e. linear, cellular, or clustered) (Weisman et al., 2008; Done et al., 2004), there have been no studies performed to determine a CAM's ability to forecast severe wind events. To develop a new metric to forecast severe wind events, it is first necessary to determine how well CAMs currently forecast severe wind events. To do this, forecasts of 10-meter wind speeds will be verified against severe wind reports for the 2012-14 period to determine CAMs' ability to forecast severe wind-producing mesoscale convective systems (MCSs). As part of the verification effort, a spatial and temporal climatology of severe wind-producing MCSs will be developed and used as verifying data. Object-based verification will be explored to determine its utility with regard to severe wind-producing MCSs.

1.2 Mesoscale Convective Systems

1.2.1 MCS Growth and Generation of Severe Wind

Houze (2004) defines a mesoscale convective system (MCS) as "a cumulonimbus cloud system that produces a contiguous precipitation area ~100 km or more in at least one direction." MCSs are also typically characterized by containing both a convective region and a stratiform region. In the stratiform region, there is usually descending air flowing towards the convective region (Houze, 2004). The rear inflow is most common with leading-line/trailing-stratiform MCSs, and "often takes a sudden plunge downward as it approaches the immediate rear of a region of active convective cells" (Houze, 2004). The "sudden plunge" is responsible for the severe winds associated with the convective region as low-θ_e air accelerates towards the surface. That is, cold air descending through an unstable environment accelerates until it reaches the ground. Schmidt and Cotton (1990) identify the source of the rear inflow as a response to gravity waves initiated by heating in the convective region. Cooling in the stratiform region due to melting, sublimation, and evaporation also contribute to the rear inflow, but Yang and Houze (1995) found that phase changes alone could not account for the strength of the strongest rear inflows. Even though gravity waves account for much of the strength of the rear inflow, Klimowski (1994) found that, even for strong MCSs, the rear inflow is weak. MCSs cannot easily develop a strong rear inflow from the combined effect of gravity waves and phase changes. If the MCS can develop vortices at the ends of a linear feature (as in a bow echo), then the rear inflow will be reinforced, especially at the apex of the bow (Skamarock et al., 1994). Skamarock et al. (1994) attributes the vortex development at the ends of the convective line to the tilting of horizontal vorticity into the vertical by the updraft along the convective line. Skamarock also found that large MCSs can develop a mesoscale convective vortex

(MCV), typically at the northern end of the convective line. In addition to the bookend vortices demonstrated in Skamarock et al. (1994), Zhang and Gao (1989) found that synoptic scale flow could also enhance the rear inflow.

Severe wind-producing MCSs have been examined (Cohen et al., 2007) on an observational basis using soundings that sample the environment of mature MCSs. Cohen et al. (2007) found that the best discriminators for distinguishing severe wind-producing MCSs from non-severe MCSs were deep-layer wind shear and upper level winds. However, Cohen et al. (2007) only examined observed soundings taken ahead of or within MCSs and not model forecasts of MCSs. No studies have systematically examined model forecasts across several years in an attempt at assessing model skill in forecasting severe wind-producing MCSs, as this study will do.

As shown in Cohen et al. (2007) and Coniglio et al. (2007), forecasting for MCSs is difficult, both when considering intensity and maintenance. Cohen et al. (2007) showed that even the best discriminators between non-severe and severe MCSs still do a relatively poor job of discriminating between the two. Coniglio et al. (2007) developed a method to determine whether an in-progress MCS would mature or weaken that takes into account deep-layer vertical wind shear, lapse rates, convective available potential energy (CAPE), and wind speeds throughout the troposphere. Though this method was initially developed using observations from maturing and weakening MCS environments, it has been extended to use model forecasts and model soundings. However, this method does not attempt to determine whether an MCS will produce severe winds at the surface. The method is most useful on the Day 1 convective outlook and watch timescales (typically 6 - ~24 hours before an event), that is, from the morning of a potential event until a few hours before the event occurs. The output of this method is conditional on an MCS occurring, so even high confidence of MCS maturation is for naught if an

MCS does not move through the area. Coniglio et al. (2007) also notes that "these concepts will likely work best on MCSs that develop and continually generate strong cold pools away from the strong larger-scale forcing when the shear and mean winds are substantial." For MCSs that are maintained by other processes, the method is less useful.

Though the current study does not focus explicitly on derechos, previous research on derechos can provide insight on severe wind-producing MCSs. Derechos are considered a subset of MCSs that produce extensive severe wind (Johns and Hirt, 1987; Corfidi et al., 2016). Johns and Hirt (1987) defines derechos based solely on severe wind reports: (a) there must be a concentrated area of reports with major axis of at least 400 km, (b) there must be a chronological sequence to the reports, (c) there must be at least three significant (>65 kt) wind reports separated by at least 64 km, and (d) successive reports can be separated by no more than three hours. Johns and Hirt (1987) also describe two types of derechos: serial and progressive. Serial derechos form with a relatively small angle between the squall line orientation and the mean wind direction, and the damage associated with serial derechos is the result of bows embedded within the system. Progressive derechos are oriented nearly perpendicular to the mean wind and are forward propagating. Due to the difference in observed severity between the two different types of derechos, Corfidi et al. (2016) has proposed a new definition of a derecho that includes a requirement of "evidence of one or more sustained bow echoes with mesoscale vortices and/or rear-inflow jets." The proposed definition removes any requirements of wind reports, but does require a nearly continuous damage swath at least 100 km wide and 650 km long. By removing the explicit severe wind report requirement, Corfidi et al. (2016) avoids issues associated with severe wind reports that will be discussed in further sections. Corfidi et al. (2016) also restricts derechos to more significant events, since mesoscale vortices and rear-inflow jets

are associated with the strongest events. Miller and Johns (2000) found that the most extreme winds associated with derechos are caused by supercells embedded within the main line rather than with a larger-scale rear-inflow jet.

1.2.2 Previous MCS Climatologies

Gallus et al. (2008) found that, between April and August 2002, linear systems accounted for 34% of the severe storm systems, but only 23% of the observed storm systems. Bow echoes generated 18.56 non-significant severe wind reports per case, and leading-line/trailing-stratiform systems generated 7.92 per case (it was found that the pattern is similar for significant severe wind reports). Gallus et al. (2008) suggests that the propensity for bow echoes and leading-line/trailing-stratiform cases to produce severe wind is due to the presence of a rear-inflow jet. The leading-line/trailing-stratiform systems likely do not produce as many severe wind reports because there is not a bookend vortex on either end, so, based on Skamarock et al. (1994), the rear inflow for leading-line/trailing-stratiform systems is weaker than it is for bow echoes. For all linear systems, Gallus et al. (2008) found that wind was the greatest threat.

Burke and Schultz (2004) examined bow echoes in the cold season (October - April) between October 1997 and April 2001 and found 51 bow echoes associated with at least one severe report (hail with diameter >0.75", tornado, or wind speed >50 kt). The first radar reflectivity echoes that would eventually become bow echoes typically occurred in the afternoon, with bow echoes forming, on average, seven hours later. The bow echoes typically dissipated two to three hours after formation. The 51 bow echoes generated 899 severe wind reports, giving an average of 17.6 severe wind reports per bow echo, which matches well with the 18.56 severe wind reports per bow echo found by Gallus et al. (2008) in the warm season of 2002. Of the 51 bow echoes, Burke and Schultz (2004) identified seven as

meeting the Johns and Hirt (1987) definition of a derecho. Burke and Schultz (2004) furthermore identified two bow echoes that generated 52 or more severe wind reports, though not meeting the minimum criteria for a derecho. These nine long-lived bow echoes "developed in strong forced, dynamic patterns with moderate instability" (Burke and Schultz, 2004). Of the 51 bow echoes, 47 formed in southwesterly flow at 500 hPa.

Smith et al. (2013) found that measured severe wind gusts associated with quasi-linear convective systems (QLCS) were most common, relative to gusts associated with supercells and disorganized convection, between November and April. The most gusts associated with QLCSs occurred in June. Measured gusts from QLCSs made up 42% of measured gusts. QLCS gusts occurred most often east of the Rockies between the plains and the Ohio River Valley.

1.3 Convection-Allowing Model Verification Efforts

Though there have been no efforts to verify 10 m wind speeds, Beck et al. (2014) used the French Doppler radar network to develop three dimensional wind fields to verify the 2.5-km French AROME model. The study, however, looked at winds 2 km above mean sea level to asses the model's skill at forecasting orographic rain events. Beck et al. (2014) found that the model forecast was skillful through its entire 48 hour forecast period. Beck et al. (2014) found that as the boundary layer approached the level at which the model was verified, the forecast got worse. This suggests that the boundary layer is a source of error within the AROME model. The Doppler wind retrieval method used in Beck et al. (2014) would be useful for verifying upper-level winds within an MCS, provided that the wind retrieval can be made with the WSR-88D network in the United States. Such a method cannot

be employed to verify 10 m wind speeds, since 10 m above ground level is below the level at which multiple Doppler analysis would be possible with the operational WSR-88D network.

Other studies attempt to extract information from convection-allowing models (CAMs). Sobash et al. (2011) generated a probabilistic forecast based on the hourly maximum of updraft helicity (Kain et al., 2008). Initially, the locations of the updraft helicity maxima were compared to the locations of the severe storm reports. This yielded poor results, since it was an attempt to have the model correctly forecast the exact location of severe storm reports. Sobash et al. (2011) notes that "point-by-point verification on a 4 km grid measures skill at predicting a severe report within 2 km of a point, so the low scores should not be surprising." Even with verification on an 80 km grid, forecast verification metrics were low. Forecast updraft helicities from the NSSL-WRF model exceeding a threshold were then converted to a probabilistic forecast using smoothing described in Hitchens et al. (2013) on an 80-km grid. All severe storm reports (hail, wind, and tornadoes) were put onto the same 80-km grid and a hindcast was generated again using Hitchens et al. (2013). The probabilistic fields were verified using a receiver operating characteristic (ROC) curve (Sobash et al., 2011). This found that the higher thresholds performed better (that is, had a higher area under the ROC curve) in distinguishing events from non-events. When comparing the forecasts on a reliability diagram, Sobash et al. (2011) found that all thresholds were reliable (that is, above the no-skill and climatology lines), but the lower thresholds tended to overforecast and the higher thresholds tended to underforecast. When fractions skill score (FSS) was used as a verification metric, Sobash et al. (2011) found that lower thresholds performed better. These results suggest that verification results can be dependent on the chosen verification metric.

Brown et al. (2007) used the Method for Object-based Diagnostic Evaluation (MODE) to verify model precipitation fields. MODE will be explained in more detail in Section 2.1, but it essentially identifies objects in both the forecast and observation field before attempting to match forecast and observed objects using a fuzzy logic algorithm. Brown et al. (2007) verified 4 km rainfall forecasts generated from a WRF model run at a 2 km grid spacing against Stage II precipitation analysis. Brown et al. (2007) found that, for analysis of a single forecast, MODE provides much more information on the forecast than other methods of verification. Brown et al. (2007) also suggests that applying MODE to many forecasts can provide a better picture of model performance. By examining severe wind events occurring in 2012 - 2014, this study will provide a more complete picture of severe wind forecasting performance by CAMs.

MODE was also used in Van der Plas et al. (2012) to verify simulated reflectivity from the Dutch 2.5-km HARMONIE model against observed composite reflectivity over western Europe. Van der Plas et al. (2012) found that the many degrees of freedom provided by MODE can result in substantial differences in object identification. This study explores a few of the degrees of freedom offered in MODE, especially in object detection. Van der Plas et al. (2012) also notes that some of the object statistics may be more useful for model intercomparisons than for a single model study.

Though not explored in this study, a version of MODE exists that is expanded into a time domain (MODE-TD) and was used by (Clark et al., 2014) to verify precipitation forecasts from a convection-allowing ensemble. This works similarly to MODE, but it finds three-dimensional (two spatial dimensions and one time dimension) objects and attempts to match forecast and observed objects. By adding time, MODE-TD is able to account and quantify errors in time as well as errors in space. MODE-TD was also used in Mittermaier and Bullock (2013) to

verify cloud-cover forecasts in the UK. MODE-TD allows for verification efforts that track the cloudy areas through the verification period. Since this study is more focused on model ability to highlight an area of potentially strong surface winds, not necessarily getting the timing correct, MODE-TD was not used.

Chapter 2

Data and Methodology

2.1 Method for Object-based Diagnostic Evaluation

An object-based verification is chosen for this study because this study is verifying a field forecast with sporadic point observations. While there are other methods to verify a field forecast with point observations, exploring object-based verification was felt to be worthwhile since no convection-allowing model verification has been done with object-based verification at the Storm Prediction Center. Additionally, object-based verification will allow for the development of a severe wind-producing MCS climatology.

The Method for Object-based Diagnostic Evaluation (MODE) is an object-based method for evaluating forecasts developed by the Developmental Testbed Center and National Center for Atmospheric Research as part of their Model Evaluation Tools (Davis et al., 2006). MODE identifies objects by applying an areal average within a user-defined radius. A user-defined intensity threshold is then applied. After the thresholding, a user-defined minimum area may be applied, with objects smaller than a certain area excluded. The resulting objects are then used to mask the original, un-convolved data (Figure 2.1).

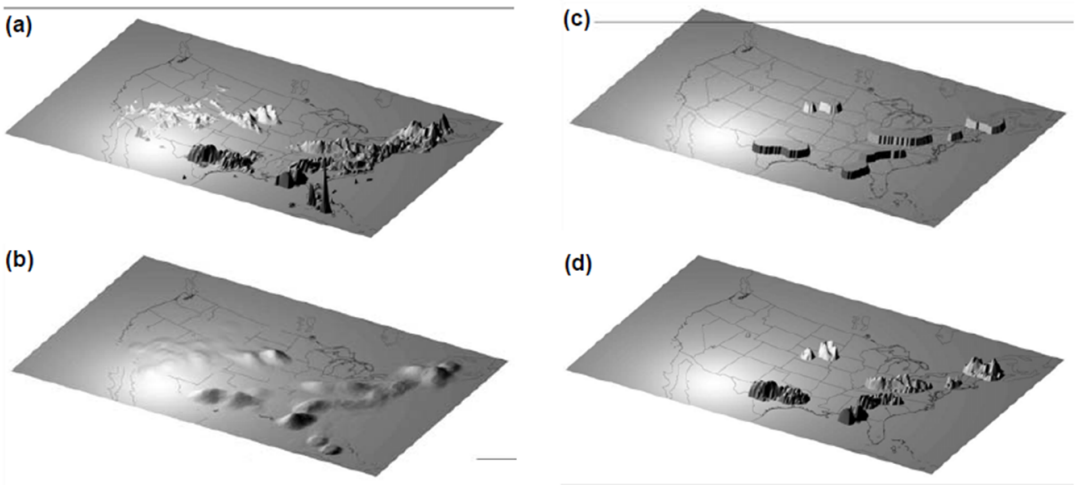

Figure 2.1: MODE process for object identification: (a) original field, (b) convolved field, (c) mask generated by thresholding convolved field, (d) applying mask to original field (Brown et al., 2007)

Once objects are identified in both the forecast and observation fields, objects in the same field may be merged via a secondary thresholding process. A second user-defined threshold is applied to the convolved field, and all objects within the new mask are merged for the purposes of later computation.

Before matching is done between forecast and observed objects, grid-based verification metrics are computed. That is, every grid square within both a forecast and observation object is counted as a hit. Every grid square within a forecast object but not an observed object is counted as a false alarm. Every grid square within an observed object but not a forecast object is counted as a miss. Every grid square in neither a forecast or observed object is counted as a correct null. This tabulation allows for the computation of grid-based verification metrics using the forecast and observed objects.

To match objects between the forecast and observed field, MODE uses a fuzzy logic engine to generate an interest score between pairs of objects. Fuzzy logic attempts to determine whether the forecast object and the observed object are the

same event. This method attempts to remove the double-penalty for spatial errors in which one missed forecast counts as both a miss and as a false alarm (Figure 2.2). A fuzzy logic engine also allows for errors to be quantified. The fuzzy logic engine in MODE computes an interest score to determine if two objects are matched. Objects are matched if their interest score is above a user-defined theshold. The formula to compute an interest score between 0 and 1, I_j, for any pair of objects, j, is given by:

$$I_j = \frac{\sum_{i=1}^{M} c_i w_i F_{i,j}}{\sum_{i=1}^{M} c_i w_i}, \tag{2.1}$$

where F_i is the interest function for attribute i; w_i is the weight assigned to attribute i; and c_i is the confidence that the interest function for attribute i is useful. Attributes and default weights for each attribute are listed in Table 2.1. The attributes are explained with Figure 2.3. The line marked (a) is the centroid distance. The boundary distance and convex hull distance are both zero, since the objects overlap. The angle between the longest axes is labeled (b). The area ratio is the ratio of the forecast and observed object areas and is approximately 1 here. The intersection area ratio is the area of the hatched region of overlap between the forecast and observation divided by the average area of the forecast and observation. The complexity ratio is the area of the object divided by the area of the convex hull. The intensity ratio takes the ratio of the forecast and observation's 70th percentile of intensity.

Attribute	Weight
Distance between centroids	2.0
Distance between boundaries	4.0
Distance between convex hulls	0.0
Angle difference between longest axes	1.0
Area Ratio	1.0
Intersection area ratio	2.0
Complexity ratio	0.0
Intensity ratio	0.0

Table 2.1: Attributes and default weights, w_i, used to calculate interest scores.

Default interest functions for each attribute are shown in Figure 2.4. Confidence values for all attributes except for angle difference and centroid distance are always equal to one. For angle difference, differences become less meaningful for nearly circular objects, as small changes in shape can cause large changes in the angle of the longest axis. Thus the confidence of angle difference, c, is a function of aspect ratio, $r = \frac{length\,of\,minor\,axis}{length\,of\,major\,axis}$:

$$c = \left[\frac{(r-1)^2}{r^2+1}\right]^{0.3}, \tag{2.2}$$

An interest score is calculated for each pair containing one forecast and one observed object. Interest scores are not calculated if the centroid distance is greater than a user-defined threshold, since objects that are very far apart are unlikely to be matched. If the interest score is greater than a user-defined threshold (default value of 0.7 used in this study), then the objects are considered matched. When computing object-based verification metrics, matched objects count as a hit, unmatched forecast objects count as false alarms, and unmatched observed objects count as misses. Correct nulls do not exist using this approach.

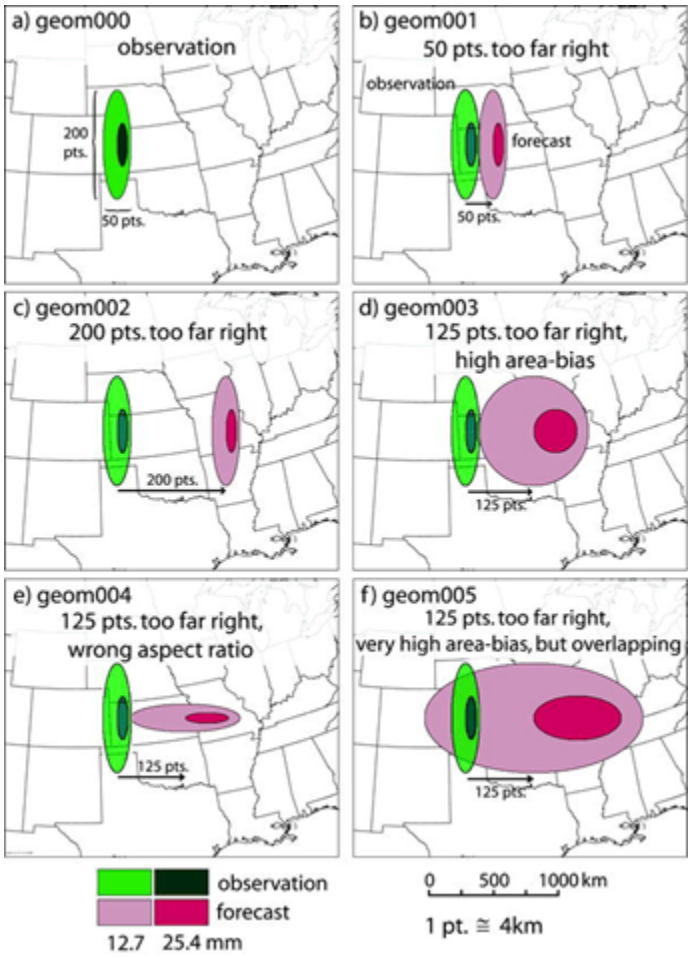

Figure 2.2: An illustration of multiple different kinds of error. (b), (c), and (e) would all score the same using grid-based verification, while (f) would score the best. A fuzzy logic engine allows (b) to score the best (Ahijevych et al., 2009).

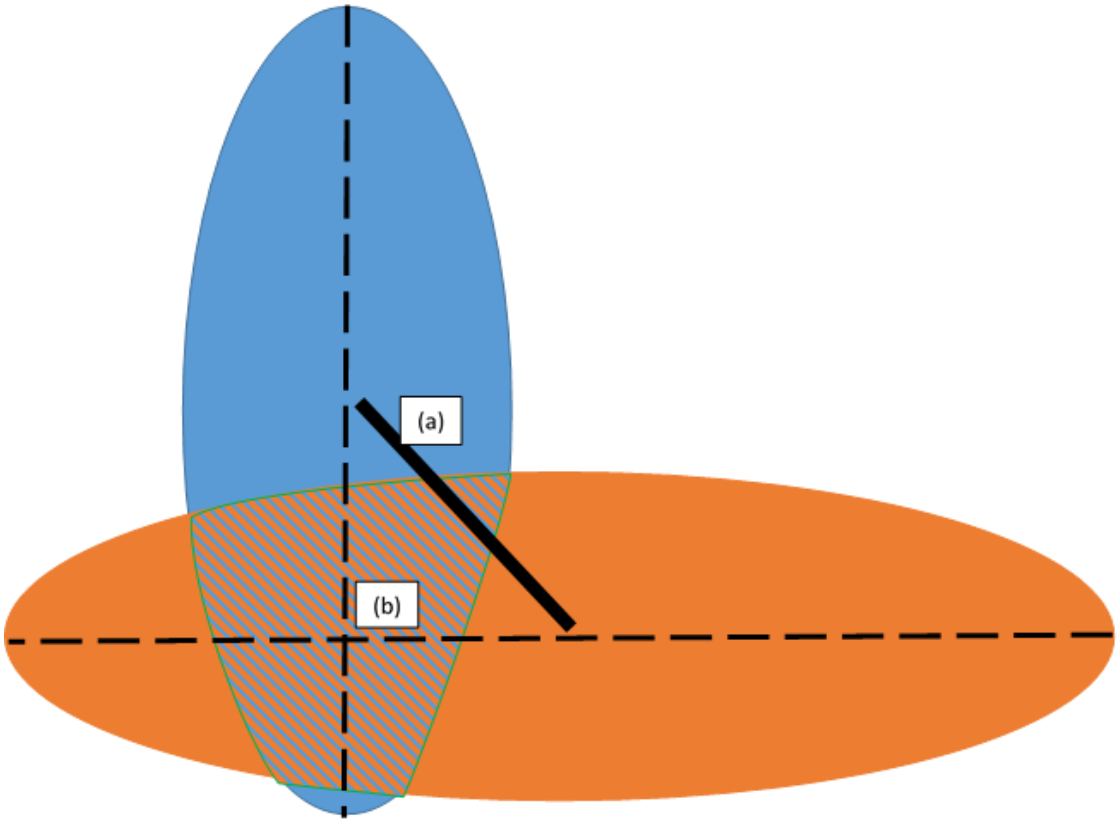

Figure 2.3: A diagram of MODE attributes. Consider a forecast in blue and observations in orange.

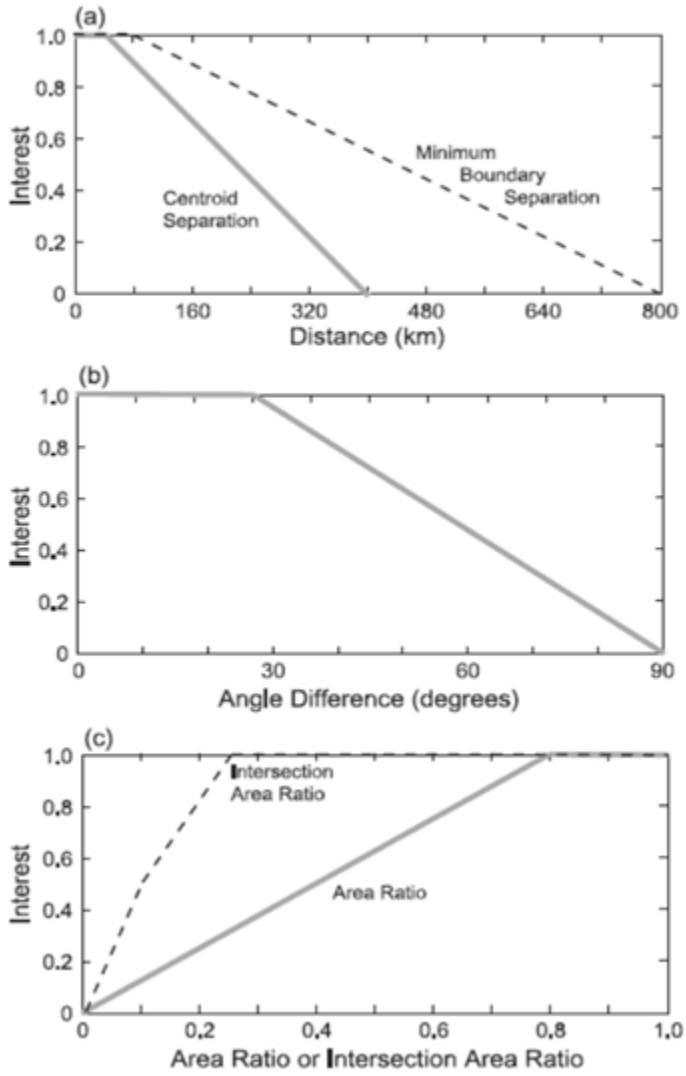

Figure 2.4: Default interest functions used in calculating interest scores based on a 4 km grid.

2.2 Severe Wind Reports

The National Weather Service defines severe wind as wind gusts greater than or equal to 50 knots (25.7 m s^{-1}, 58 mph). Severe wind reports accounted for 65% of all severe local storm reports (hail with diameter >1", wind speed >50 kts, or a tornado) from 2012 through 2014. Local storm reports are collected by NWS Weather Forecast Offices (WFOs) from 12Z on one day through 1159Z on the next day (referred to as a convective day, hereafter all references to days are referring to convective days). Depending on the time of year and region of the country, this roughly corresponds to the 24-hour period beginning at or just before sunrise. Sunrise is the approximate daily minimum of severe storm reports (Kelly et al., 1985), so the number of events occurring across two convective days is minimized.

Wind reports are initially collected in the immediate aftermath of an event by local NWS WFOs along with tornado and severe hail reports. The local WFO then removes duplicate reports of the same event and reports that were unsubstantiated and collects additional information about the event through storm surveys. These reports are collected in NOAA's *Storm Data* publication. There are several minimum criteria for inclusion in *Storm Data*: damage greater than $500,000, at least one significant report (wind speed greater than 65 kt or hail with diameter greater than 2"), or any death or injury (Trapp et al., 2006). While the local storm reports may include wind speed, there is no indication whether the speed is measured or estimated. *Storm Data* reports include wind speed for all reports, including whether the speed was measured or estimated. Since wind speeds are often overestimated (Doswell et al., 2005), measured wind reports in *Storm Data* are used as another potential way to identify severe wind-producing MCSs. Additionally, *Storm Data* wind reports that meet or exceed the NWS's significant wind threshold of 65 kt (33.4 m s^{-1}, 75 mph) are used as another potential way to identify severe wind-producing MCSs.

In addition to the magnitude overestimation issues shown in Doswell et al. (2005), there are other issues with severe reports. As described in Doswell and Burgess (1988), for a report to show up in the local storm report or *Storm Data* databases, three things must happen: someone must observe the event, they must recognize that the event meets the severe criteria, and they must report the event to the relevant authority. This leads to potential population biases, since it is less likely someone will observe the event if there is low population density except for near roads (Weiss et al., 2002). Weiss also mentions diurnal biases, since it is more difficult to observe events at night. Additionally, the use of wind damage reports can introduce biases. As Trapp et al. (2006) notes, a report of "trees were downed" could be "a few bent-over saplings, a large grove of snapped hardwood trees with ~0.5 m diameters, or something in between." Trapp also notes that report (either local storm report or *Storm Data*) concentration or counts do not necessarily correlate with wind speed magnitude. An event that had only three local storm reports resulted in $1 million in damages from 70 mph wind gusts, while an event with 55 reports resulted in only $0.3 million in damages with less significant damage than the other case (Trapp et al., 2006). The lack of correlation between reports and monetary damages is not an issue for this study. The lack of correlation between reports and wind magnitude is still an issue in this study, but subsets of reports that are more directly correlated with wind speed will be explored.

2.3 NSSL-WRF

The 10 m wind forecasts were generated from a 4-km grid spacing configuration of the Weather Research and Forecasting model (WRF) run by the National Severe Storms Laboratory (NSSL, the model is hereafter referred to as the NSSL-WRF)

initialized at 00Z and run to 36 hours (until 12Z the next day). The NSSL-WRF uses Mellor-Yamada-Janjić boundary layer and turbulence parameterization (Mellor and Yamada, 1982), WRF Single-Moment 6-Class microphysics (Hong and Lim, 2006), Rapid Radiative Transfer Model longwave radiation (Mlawer et al., 1997), Dudhia (1989) shortwave radiation, Noah land surface model (Chen and Dudhia, 2001). The NSSL-WRF has 35 vertical levels, a 24 second time step, and uses NAM output interpolated to a 40-km grid for initial and boundary conditions.

Since 10 meters above ground level is well within the boundary layer, 10 m winds will be directly affected by the boundary layer scheme. The MYJ scheme is a local scheme that uses 1.5 order turbulence closure using turbulent kinetic energy (Janjić, 1990). The TKE balance equation used is:

$$\frac{d}{dt}(\frac{q^2}{2}) - \frac{\partial}{\partial z}[lqS_q(\frac{\partial}{\partial z})\frac{q^2}{2}] = P_s + P_b - \epsilon, \tag{2.3}$$

where $\frac{q^2}{2}$ is turbulent kinetic energy and P_s, P_b, and ϵ are shear production, buoyant production, and dissipation of turbulent kinetic energy, respectively. The production terms, P_s, P_b, and ϵ, are computed by:

$$P_s = -\overline{wu}\frac{\partial U}{\partial z} - \overline{wv}\frac{\partial V}{\partial z}, \tag{2.4}$$

$$P_b = \beta g\overline{w\theta_v}, \tag{2.5}$$

$$\epsilon = q^3(B_1 l)^{-1}, \tag{2.6}$$

where B_1 is an empirical constant and u, v, and w are the zonal, meridional, and vertical components of the wind, respectively. The covariances in Equations 2.4 and 2.5 are given by eddy diffusivity, with the eddy diffusivity coefficient a function of the master length scale, l, TKE, wind shear, and atmospheric stability.

The master length scale, l, is given by:

$$l = l_0\kappa z(\kappa z + l_0)^{-1}, \tag{2.7}$$

$$l_0 = \alpha[\int_{p_T}^{p_S} |z|q\,dp][\int_{p_T}^{p_S} q\,dp]^{-1}, \tag{2.8}$$

where α is an empirical constant, κ is the von Karman constant, and p_S and p_T are the pressures at the lowest and highest model levels, respectively.

For the surface layer, the MYJ scheme uses a method that performs similarly to Monin-Obukhov similarity theory (Janjić, 1990). It is derived by assuming that TKE production and dissipation are exactly balanced in the layer between the surface and the lowest layer of the model. The resulting profile of meteorological variables between z_0, which is given over land as:

$$z_0 = 0.1 + 0.00001\Phi_s, \tag{2.9}$$

where Φ_s is the surface geopotential, and the lowest model level is shown in Figure 2.5. Since the lowest model level is above 10 meters, 10 m wind speed is derived based on this profile for u and v winds.

2.4 Event Identification

To use MODE to objectively verify model forecasts, it was first necessary to figure out how to best identify severe wind-producing MCSs that occurred during 2012-14. Initially, this was done manually using severe wind reports and radar reflectivity, then the manually identified severe wind-producing MCSs were used to determine the best objective approach to identify severe wind-producing MCSs using MODE.

2.4.1 Manual Identification

Using the Storm Prediction Center's Severe Weather Events Archive (Carbin et al., 2016), events were identified in 2012-2014 if 15 or more local storm reports occurred within 3 hours and 100 km of each other per mesoscale convective system (MCS) criteria from Parker and Johnson (2000). This yielded 264 days on which severe wind swaths occurred over the three-year period. These 264 days were examined

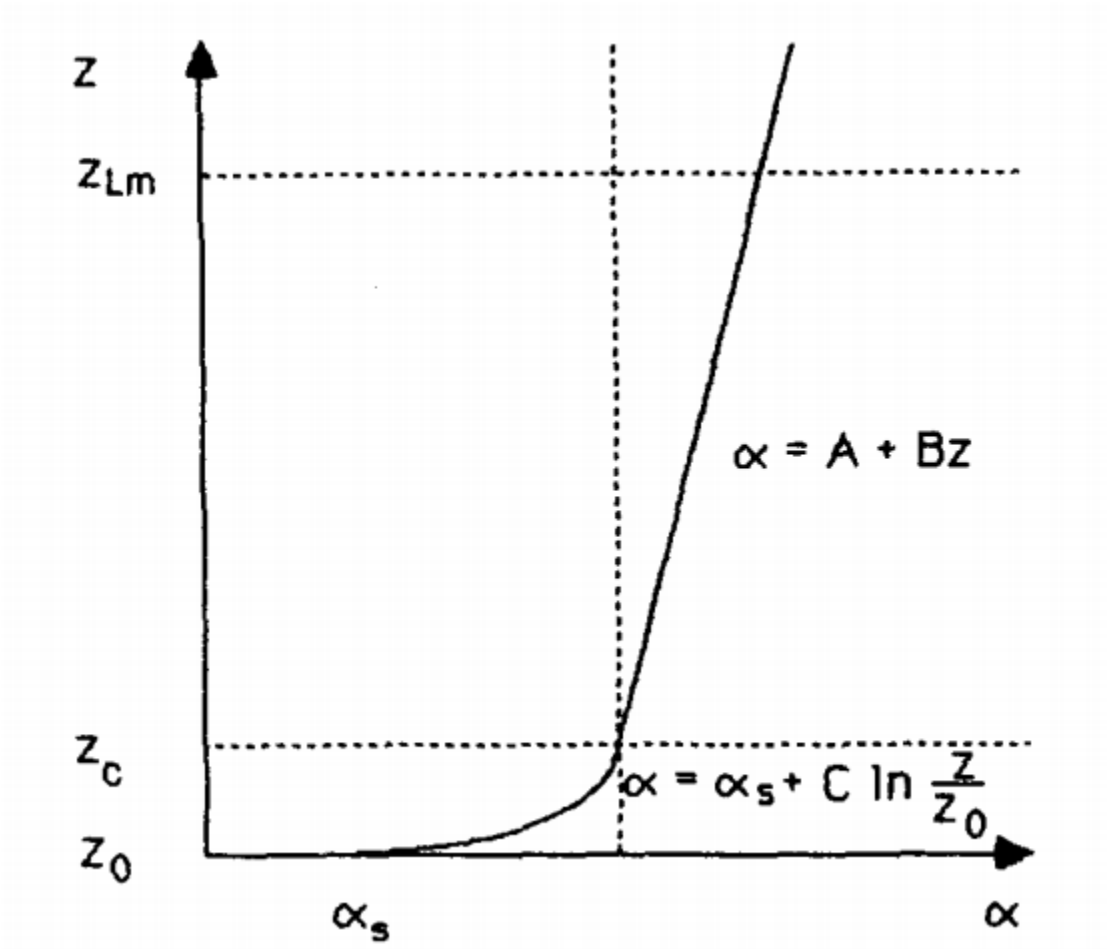

Figure 2.5: Profile shape of meteorological variables between z_0 and the lowest model level, z_{Lm}. The height of the dynamical turbulence layer is z_c, the roughness height is z_0. A, B, and C are constants. α is any meteorological variable and α_s is the value of α at the surface. (Janjić, 1990, Figure 4)

further with the Severe Weather Events Archive to determine if the wind swaths were co-located with organized convective structure in radar reflectivity that occurred for at least three hours to identify severe wind-producing MCSs. The dates and approximate centroids of the resulting 224 severe wind-producing MCSs were recorded.

2.4.2 MODE Identification of Severe Wind Events

To identify a coherent damaging wind swath from severe wind-producing MCSs, it was necessary to apply a spatial Gaussian kernel density estimation to the severe wind reports. This was done using the practically perfect method described in Hitchens et al. (2013) modified to be used on a 4-km grid. Hitchens et al. (2013) used an 80 km grid with a 120 km Gaussian smoother. All grid squares containing a report were assigned a value of 1 and the Gaussian smoother was applied to produce a probabilistic field that should match what a Storm Prediction Center forecaster would forecast given perfect foreknowledge of the day's severe storm reports. The modification to the practically perfect method was to put all severe wind reports on a 4-km grid and assign a value of 1 to all grid squares within a 10 grid square (40 km) radius of a wind report. The same 120 km Gaussian smoother was applied. All storm reports for 29 June 2012 are shown in Figure 2.6, and the practically perfect hindcast for severe wind are shown in Figure 2.7.

Due to the potential issues with severe wind reports and to eliminate severe wind reports not associated with MCSs, it was decided to use observed radar reflectivity to eliminate reports not associated with large regions of organized convection. Reports were discarded if they were not within 40 km of a contiguous area of radar reflectivity greater than 35 dBZ covering 500 grid square (8000 km^2 on a 4 km grid). The 35 dBZ radar reflectivity threshold was chosen to capture convective radar echoes as in Mecikalski and Bedka (2006). The 40 km radius of

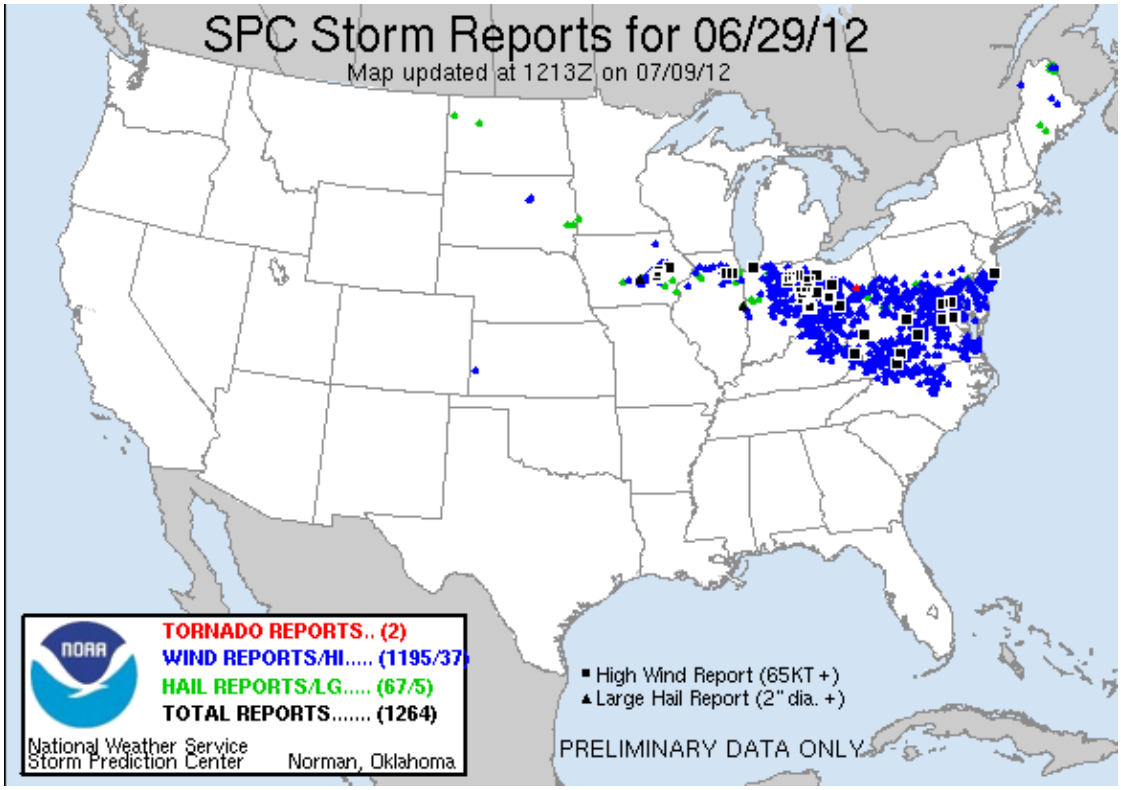

Figure 2.6: All local storm reports for the 29 Jun 2012 convective day. Wind reports are blue dots, and significant wind reports are black squares.

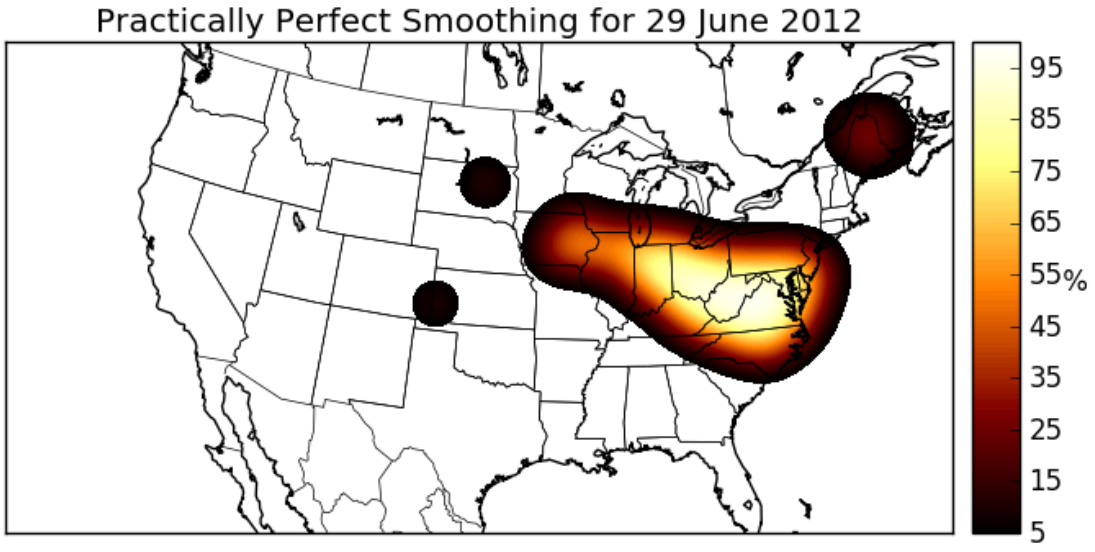

Figure 2.7: Practically perfect smoothing of unfiltered local storm reports for 29 June 2012.

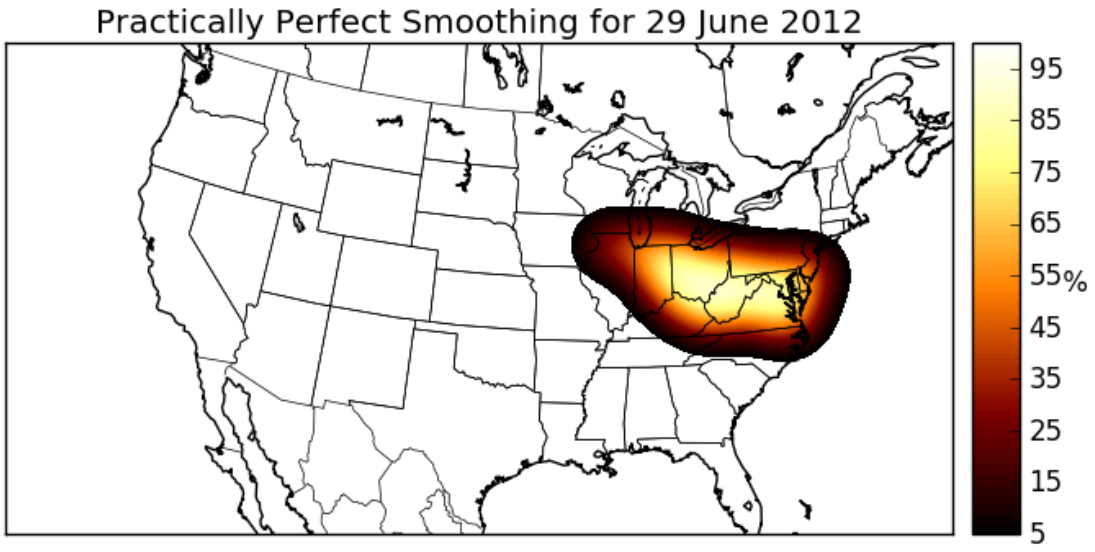

Figure 2.8: As in Figure 2.7, but for local storm reports filtered by radar reflectivity.

influence was chosen to account for wind reports caused by outflow boundaries and gust fronts and to match Hitchens et al. (2013). The 8000 km^2 minimum area represents a circle with a ~100 km diameter. This minimum area ensures that the area of radar reflectivity is larger than 100 km in at least one direction to match Parker and Johnson (2000). An example of the practically perfect hindcast for severe wind reports filtered by radar reflectivity is shown in Figure 2.8. The three areas of probabilities in Maine, South Dakota, and Kansas seen in Figure 2.7 were eliminated in Figure 2.8 because the reports were not associated with an area of reflectivity large enough to trigger the radar filter.

The practically perfect methodology was applied for each day in the study period (2012 - 2014) to all local storm reports, local storm reports filtered by radar reflectivity, *Storm Data* reports filtered by radar reflectivity, measured from *Storm Data*, and significant reports from *Storm Data*. Severe wind objects were identified using MODE with various convolution and minimum area thresholds. MODE-identified objects were then compared with manually identified severe wind-producing MCSs.

To determine which wind report subset and MODE parameters identified objects that best matched the manually identified severe wind-producing MCSs, the centroids of MODE objects were compared to the manually identified severe MCS centroids described in Section 2.4.1. MODE-identified objects within 2 degrees of latitude and longitude of a manually identified object counted as a hit. Two degrees was chosen to account for errors in manually identified centroids and reports early in or near the end of the MCS's life cycle that may have been discarded by the radar filter. Unmatched MODE-identified objects counted as a false alarm and unmatched manually identified objects counted as a miss. Results from all report types, convolution thresholds, and minimum area thresholds were plotted on a performance diagram (Roebber, 2009) to determine which MODE parameters and report filtering best identified objects that matched manually identified severe wind-producing MCSs.

2.4.3 Climatology of Severe Wind-Producing MCSs

Once the wind report type and MODE parameters were found that best matched the manually identified severe wind-producing MCSs, a spatial climatology was developed using MODE-identified objects. Spatial seasonal climatologies were also developed for December, January, and February (DJF); March, April, and May (MAM); June, July, and August (JJA); and September, October, and November (SON).

To develop a temporal climatology, the number of severe wind-producing MCSs expected on a day, C_j, was calculated by:

$$C_j = \frac{\sum_{i=j-M}^{j+M} N_i}{2M+1}, \tag{2.10}$$

where j is the ordinal date (wrapping around 365 when necessary), M is either 15 (for monthly calculations) or 45 (for seasonal calculations), and N_i is the number of severe wind-producing MCSs that occurred on ordinal date i.

2.5 Verification of NSSL-WRF

A 24-hour maximum 10 m wind field was created by taking the maximum of the 24 individual hourly maximum 10 m wind fields from forecast hours 12 through 36 (i.e. from 12Z to 12Z for a 00Z forecast, a convective day). A simulated radar filter was applied that matches the observed reflectivity filter that was applied to wind reports: areas of model forecast wind were discarded if they were not within 40 km of an area of 500 contiguous grid squares of simulated hourly maximum reflectivity higher than 35 dBZ. An example of a forecast field both before and after the application of the radar filter applied are shown in Figures 2.9 and 2.10, respectively.

It was necessary to apply practically perfect smoothing to the forecast field so that forecast and observed objects would have similar characteristics and could be compared using MODE. To generate practically perfect fields, thresholds were applied to the forecast field at various wind speeds between 15 and 60 kts (7.7 - 30.9 m s^{-1}). Areas with forecast wind speeds higher than the threshold were assigned a value of 1 and all other areas assigned a value of 0. The same practically perfect smoothing was applied as was applied to the reports: 1) All grid squares within 40 km of an area of wind speeds above the threshold were given a value of 1 and 2) a 120 km Gaussian smoother was then applied to create a probabilistic field. A selection of practically perfectly smoothed forecasts based on the filtered wind field are shown for several wind speed thresholds in Figure 2.11.

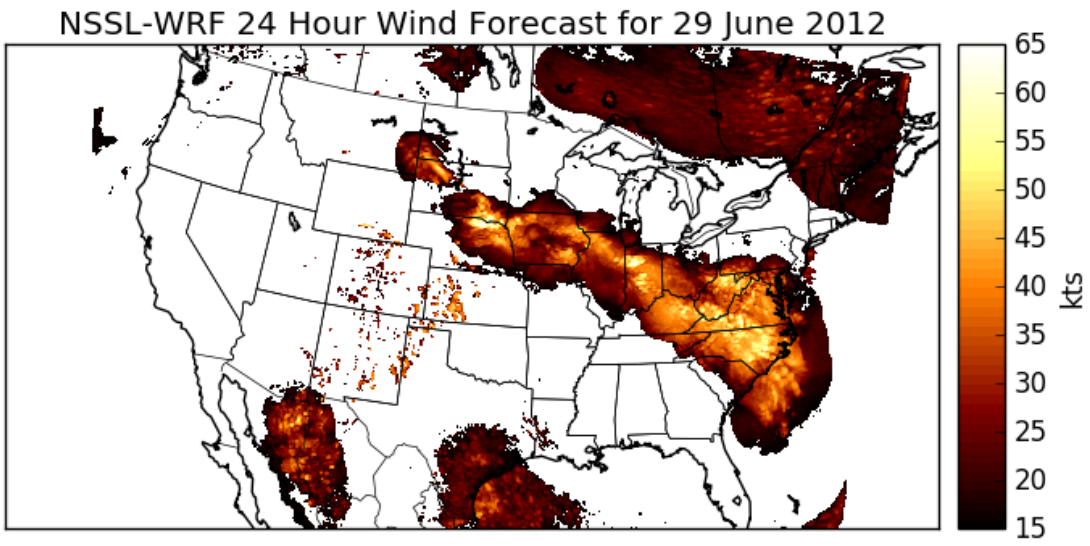

Figure 2.9: NSSL-WRF 10 m 24 hour maximum wind field without the radar filter. Note the winds in the Rocky Mountains, western Kansas, and the panhandles of Oklahoma and Texas.

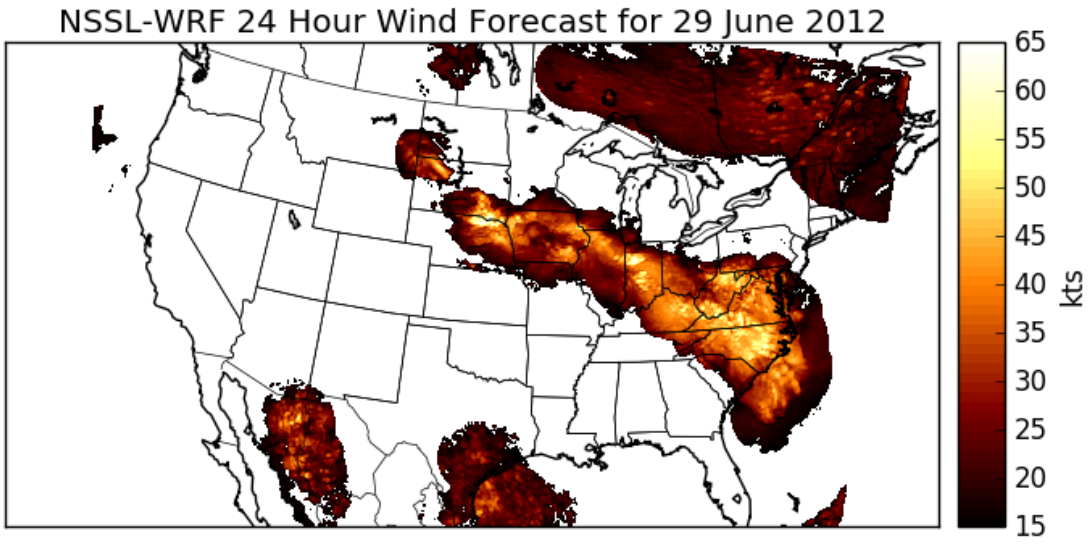

Figure 2.10: NSSL-WRF 10 m 24 hourly maximum wind field with the radar filter applied.

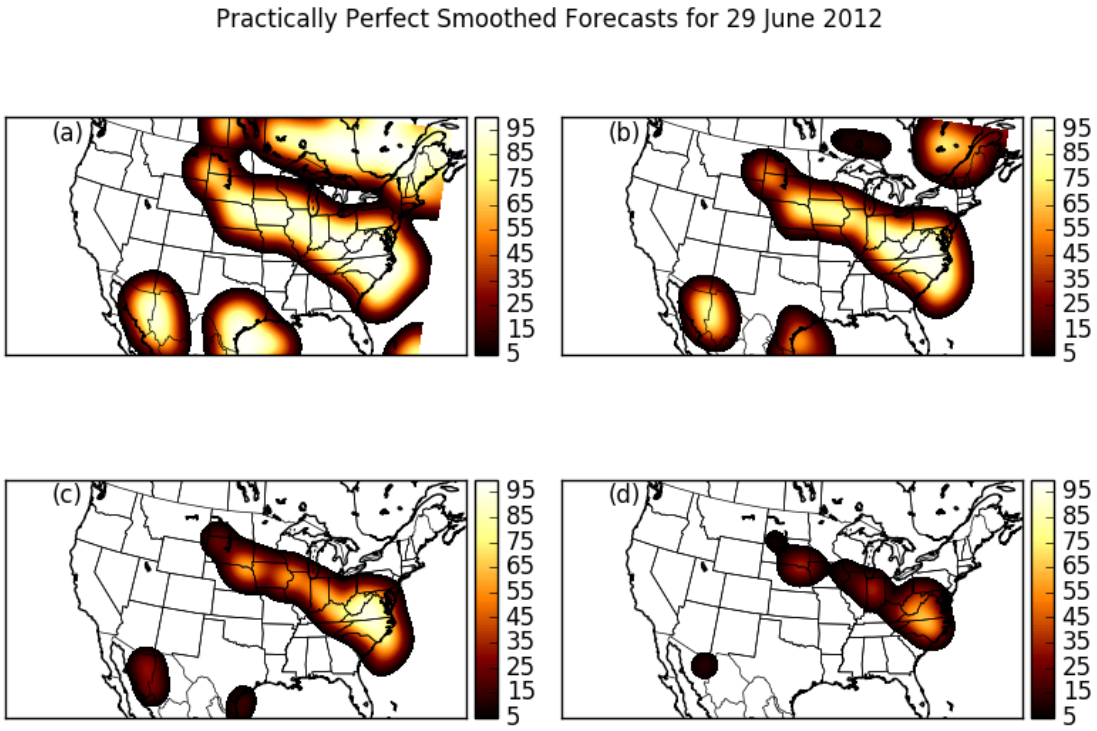

Figure 2.11: Practically perfect forecasts for (a) 20 kt, (b) 30 kt, (c) 40 kt, and (d) 50 kt thresholds based on the reflectivity-filtered wind forecast in Figure 2.10.

As discussed in Section 2.1, verification metrics were computed in two ways. Additionally, to determine the utility of using MODE, traditional grid-point verification statistics were computed. For this traditional grid-point verification, radar-filtered local storm reports were plotted on a 4-km grid, and hits were counted if the forecast wind speed exceeded a threshold in the same grid square as a report. Misses were counted if the forecast wind speed exceeded a threshold, but there was no wind report in the grid square. False alarms were counted if there was a wind report in a grid square, but forecast wind speed did not exceed a threshold. Correct nulls were counted if there was neither a wind report or wind speeds exceeding a threshold in a grid square. Verification results are presented in a performance diagram (Roebber, 2009). A performance diagram plots success rate on the horizontal axis and false alarm rate on the vertical. Lines of constant bias are straight lines that go through the origin with their slope equaling the bias. On performance diagrams presented here, only the line of bias = 1 will be shown as a dashed line. Lines of constant critical success index are curved. The relationships between critical success index (CSI), bias, probability of detection (POD), and success rate (SR) are:

$$POD = \frac{hits}{hits + misses}, \tag{2.11}$$

$$SR = 1 - \frac{false\,alarms}{hits + false\,alarms} \tag{2.12}$$

$$CSI = \frac{1}{\frac{1}{SR} + \frac{1}{POD} - 1}, \tag{2.13}$$

$$bias = \frac{POD}{SR} = \tan\theta, \tag{2.14}$$

where θ is the angle between the horizontal axis and the bias line.

Chapter 3

Observed Severe Wind-Producing MCSs

3.1 Comparison of Report Filtering

Results of event identification using all local storm reports are shown in Figure 3.1. As the minimum area threshold increases for a given convolution threshold, both the probability of detection (POD) and false alarm rate (FAR) decrease. This is because increasing the minimum area threshold results in the identification of fewer objects, so fewer hits and fewer false alarms occur. As the convolution threshold increases for a given minimum area threshold, FAR decreases. With the smallest area threshold, increasing the convolution threshold initially increases POD before decreasing. For larger minimum area thresholds, increasing the convolution threshold decreases the POD. The general trend of decreasing FAR and POD with increasing convolution threshold is because increasing the convolution threshold identifies smaller objects, which are then more likely to be excluded by the minimum area threshold. The slight increase in POD with increasing convolution threshold at the smallest minimum area threshold is likely because the centroids of the very large objects detected were more likely to be more than 2 degrees of latitude and longitude away from the manually identified centroids. The maximum critical success index (CSI) is 0.43, and occurs with a bias near 1 for 45% and 3000 grid square (48000 km^2) thresholds.

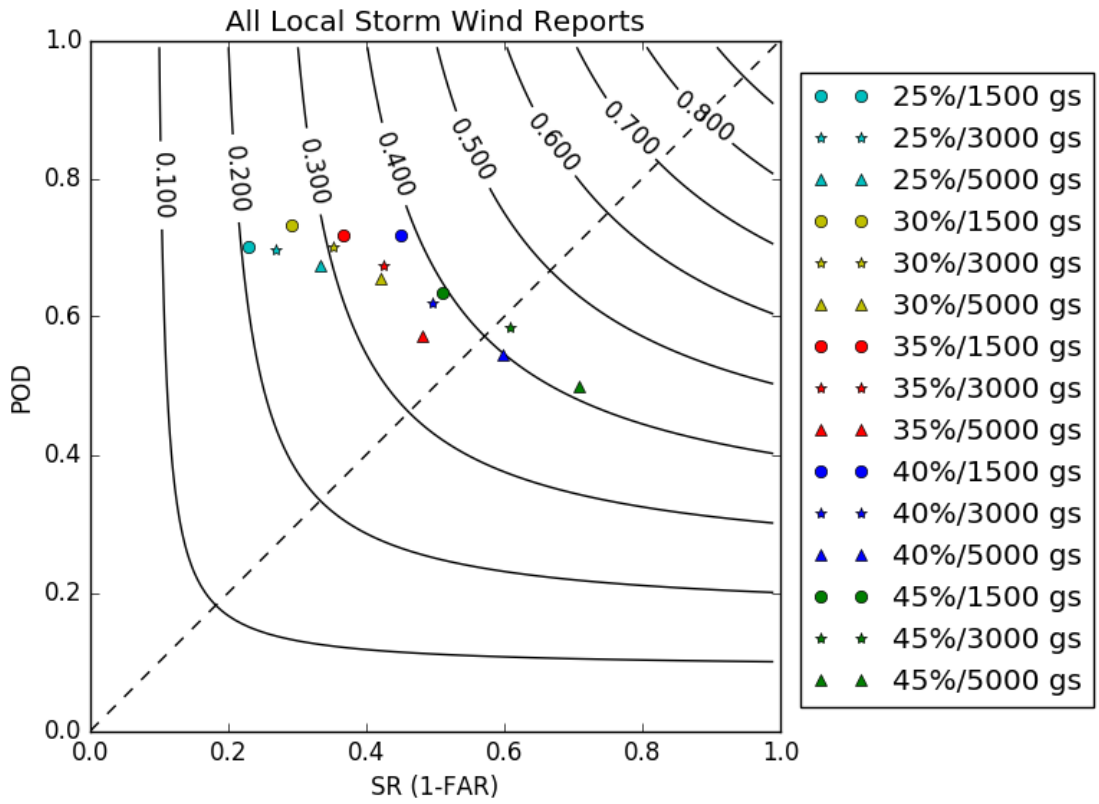

Figure 3.1: Performance diagram showing results of object identification when using all local storm reports of wind. 'gs' are grid squares on a 4-km grid. A perfect identification would be in the top right corner. Common intensity thresholds are represented by the same color, and common minimum area thresholds are represented by the same shape. For object identification, the goal is to maximize CSI and have bias be as near to 1 as possible.

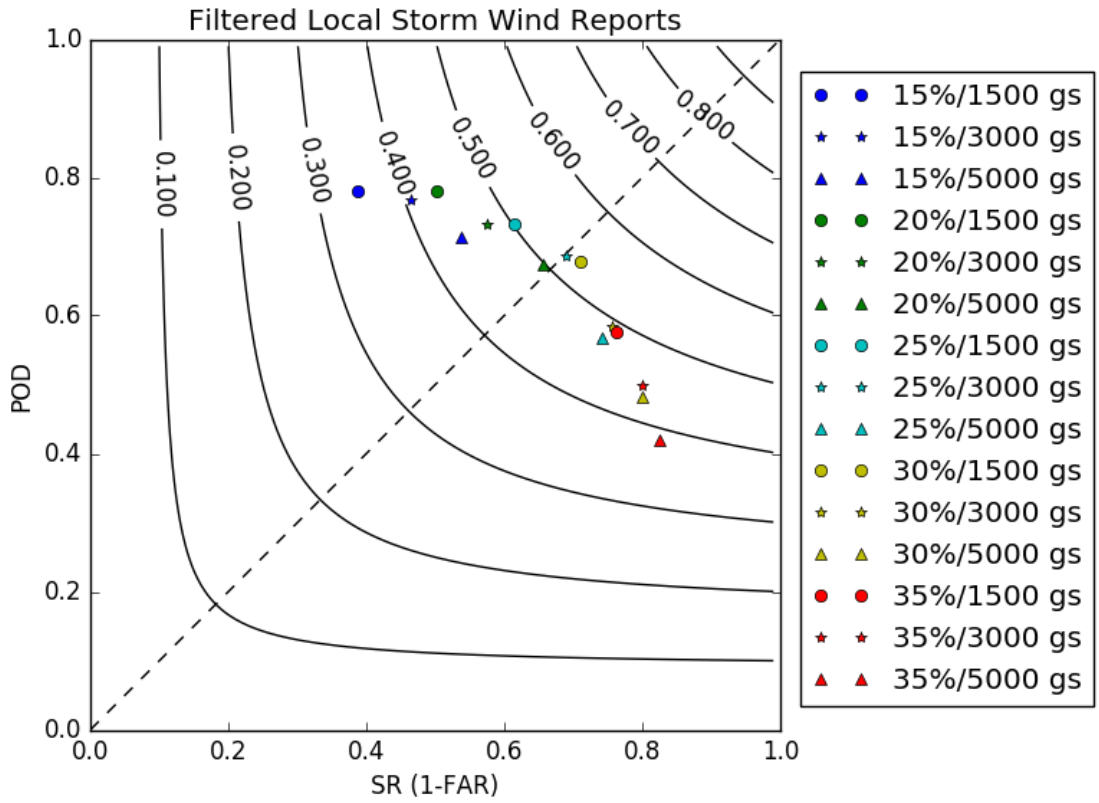

Figure 3.2: As in Figure 3.1, but for filtered local storm wind reports.

When using local storm wind reports filtered by radar reflectivity, CSI improves when compared to unfiltered reports (Figure 3.2). The improvement mostly comes via a reduction in FAR because there are fewer filtered reports, so there are fewer objects identified when using filtered reports. The objects that are identified match just as well with the manually identified objects as the objects identified using unfiltered reports. Thus, the radar filtering performed as intended, by removing wind reports and not detecting objects not associated with MCSs. As with the unfiltered reports, increasing convolution and minimum area thresholds decrease both POD and FAR. The maximum CSI, which again occurs when the bias is nearly 1, is 0.53, with a 25% convolution threshold and a 3000 grid square (48000 km^2) minimum area threshold.

Since the local storm wind reports filtered by radar reflectivity performed better than unfiltered local storm wind reports, *Storm Data* wind reports filtered using observed radar reflectivity were compared with local storm wind reports filtered by radar reflectivity. As can be seen in Figure 3.3, both local storm and *Storm Data* wind reports have a bias near 1, but local storm wind reports have a slightly higher CSI than *Storm Data* wind reports. Tables 3.1 and 3.2 show numbers of objects correctly and incorrectly identified for *Storm Data* and local storm wind reports, respectively. Since local storm wind reports and *Storm Data* wind reports should be nearly identical, a Monte Carlo simulation was done to determine whether the results produced by the two reports were statistically significantly different. A Monte Carlo simulation randomly simulates the event many times to determine if differences are significant or not.

The Monte Carlo simulation randomly simulated a 224 object forecast 1000 different times. The probability of a correct forecast and the probability of a false alarm in the simulated forecasts was equal to the FAR and POD for *Storm Data* wind reports. The number of times out of the 1000 simulated forecasts that the simulated forecast had more hits or fewer false alarms than the local storm wind reports was counted. The random forecast had more hits than the local storm wind reports 18.2% of the time and had fewer false alarms than the local storm wind reports 28.8% of the time. Neither of these approach the 95% threshold necessary for the difference between *Storm Data* and local storm wind reports to be statistically significant.

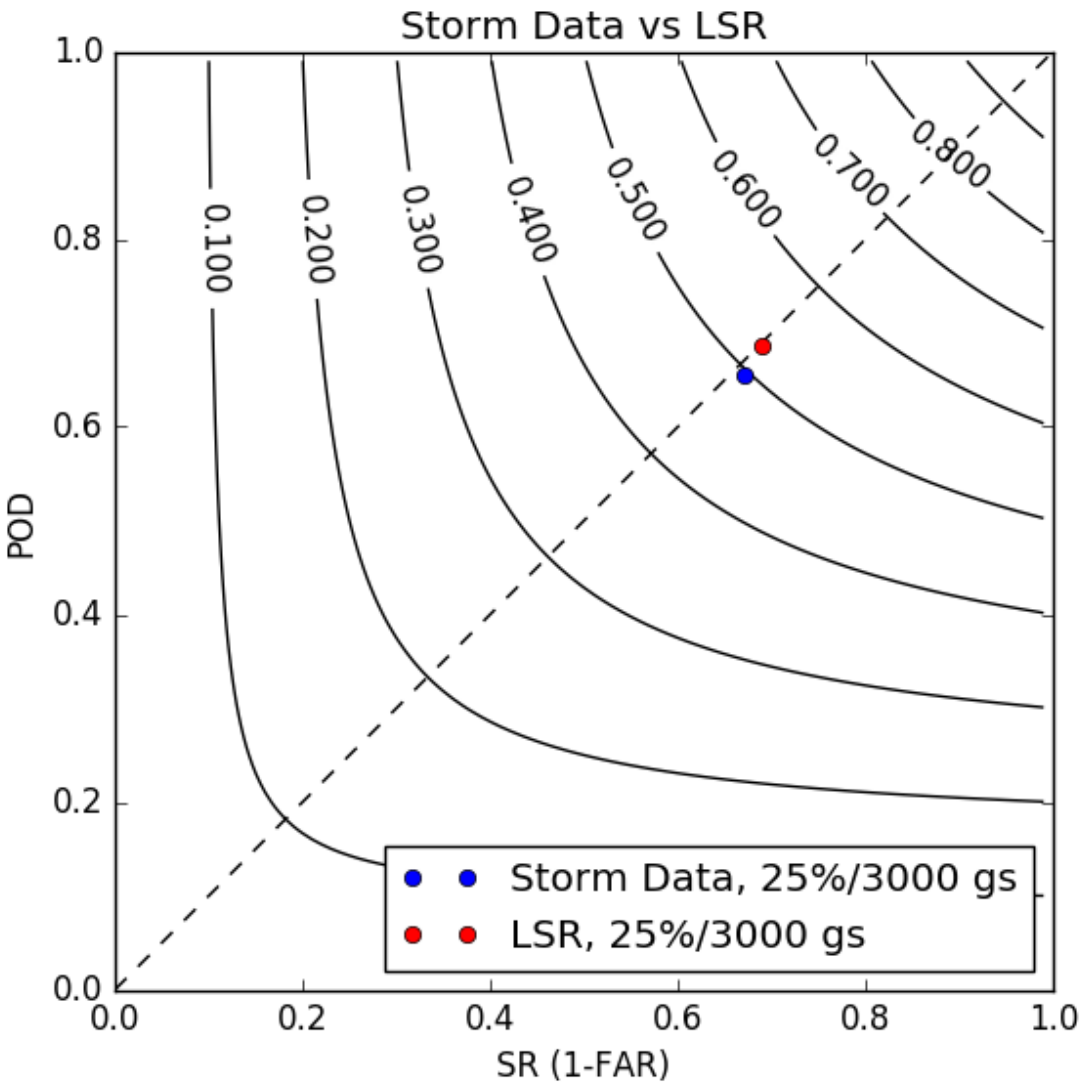

Figure 3.3: Performance diagram comparing the results of *Storm Data* wind reports and local storm wind reports (LSR).

	Manually Identified Yes	Manually Identified No
MODE Identified Yes	147	72
MODE Identified No	77	Not counted

Table 3.1: Contingency table showing object identification results for *Storm Data* wind reports.

	Manually Identified Yes	Manually Identified No
MODE Identified Yes	154	69
MODE Identified No	70	Not counted

Table 3.2: As in Table 3.1, but for local storm wind reports

Measured *Storm Data* wind reports, not filtered by radar, provide an alternate way to avoid spurious wind damage reports that may not be associated with winds above the severe wind threshold (50 kts, 58 mph, 25.7 m s^{-1}). Results of object identification using measured *Storm Data* wind reports are shown in Figure 3.4. Though FAR is much lower than for filtered local storm wind reports, POD is also significantly lower. Across all thresholds, CSI is much lower, with the maximum CSI of 0.40 for the 15% and 3000 grid square thresholds. CSI is much lower because there are fewer objects identified than with all or radar filtered storm reports. Additionally, unlike the filtered local storm wind reports, the maximum CSI did not occur with a bias near one. The poorer performance of measured *Storm Data* wind reports is because measured reports account for only 2% of all wind reports (Smith et al., 2013), so the magnitude of practically perfect probabilities is lower, which means fewer objects are identified.

Significant *Storm Data* wind reports (wind speed $\geq$ 65 kts), not filtered by radar, may provide an even better way to avoid spurious wind damage reports

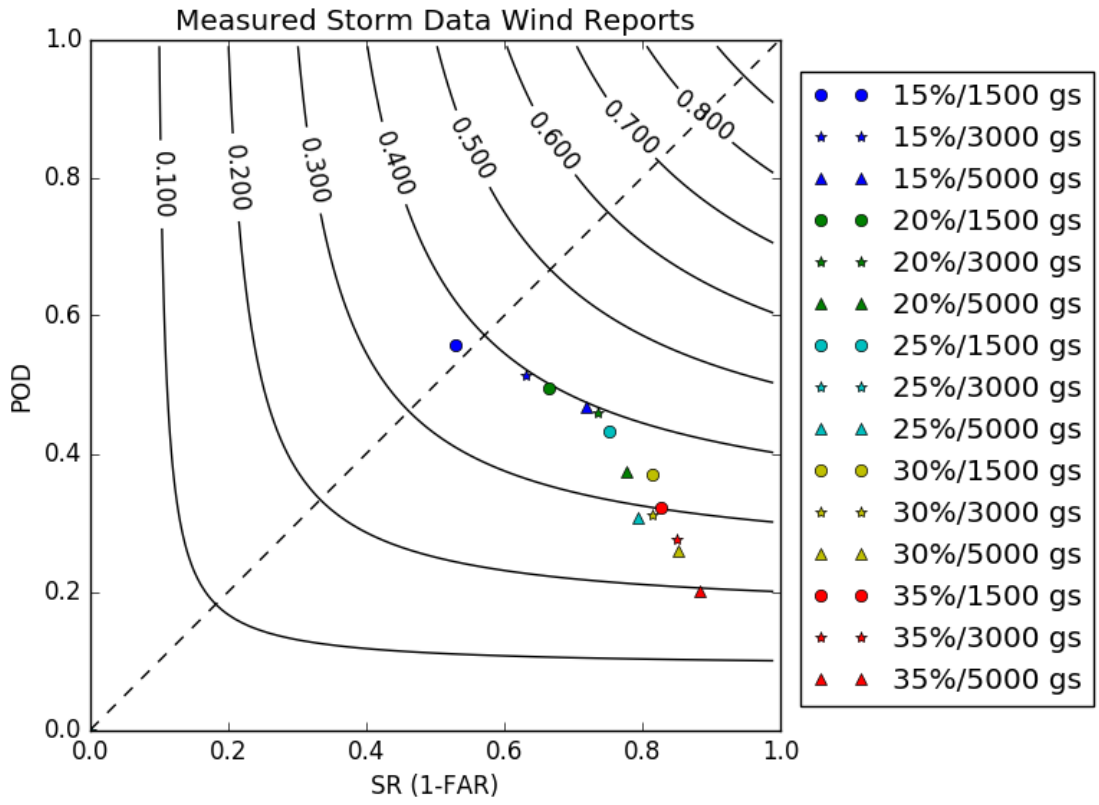

Figure 3.4: As in Figure 3.1, but for measured *Storm Data* wind reports.

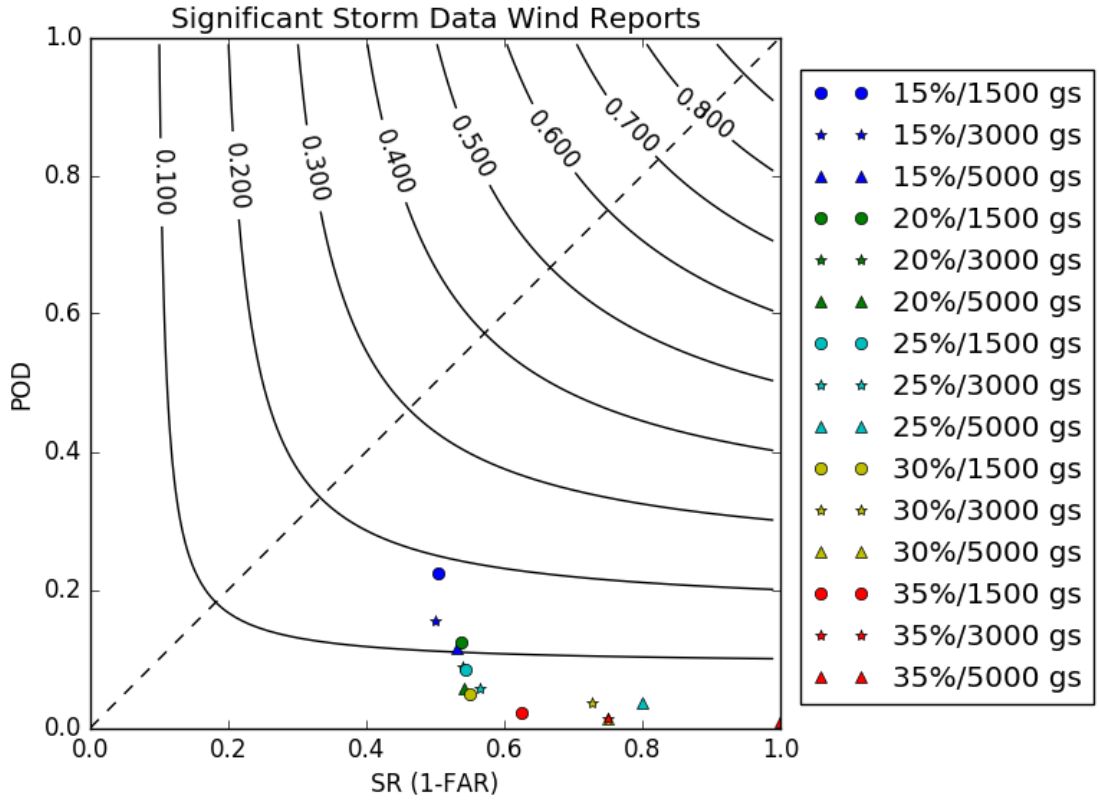

Figure 3.5: As in Figure 3.1, but for significant *Storm Data* wind reports.

because 65 kts is a more stringent condition than the 50 kt threshold for severe wind. Results of object identification using *Storm Data* wind reports are shown in Figure 3.5. POD and FAR are much lower then for both measured *Storm Data* wind reports and filtered local storm wind reports. The maximum CSI is 0.18 with the 15% and 1500 grid square (24000 km^2) thresholds. The low CSI is a result of significant *Storm Data* wind reports being a further subset of measured *Storm Data* wind reports. This means the low practically perfect magnitudes and small object drawbacks with measured *Storm Data* wind reports are exacerbated. In fact, at the highest threshold (35% and 5000 grid squares), only two objects were detected, and the most objects were detected at the lowest threshold: 15% and 1500 grid squares detected 99 objects.

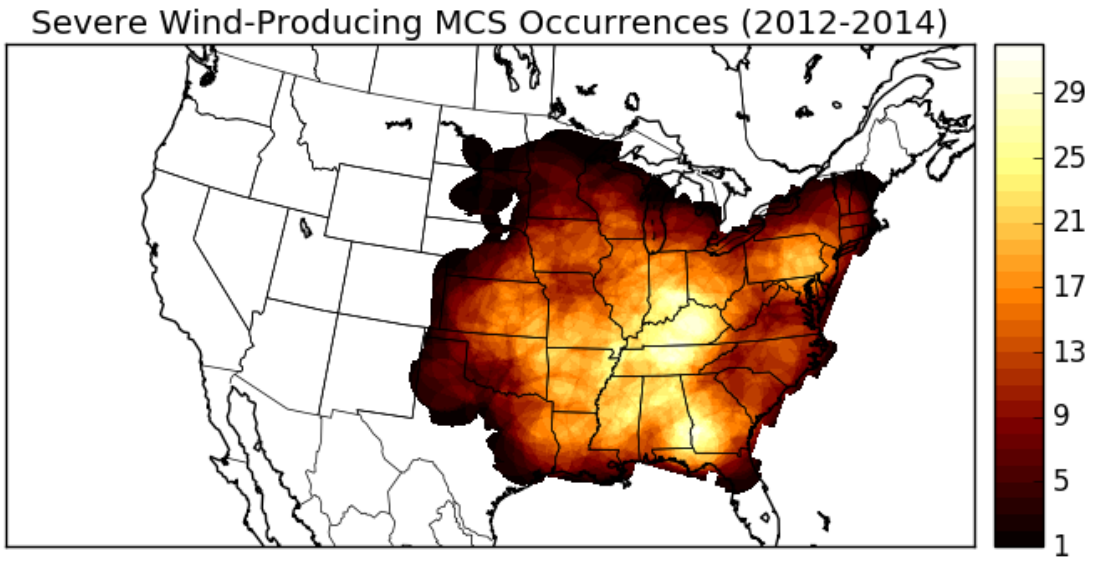

Figure 3.6: Observed severe wind-producing MCSs.

Based on these results, radar-filtered local storm wind reports with a 25% convolution threshold and 3000 grid square minimum area threshold were used to identify observed severe wind-producing MCSs.

3.2 2012-2014 MCS Occurrences

The locations of all MODE-identified severe wind-producing MCSs are shown in Figure 3.6. The distribution of severe wind-producing MCSs is similar to that shown in Smith et al. (2013). There are two maxima with more than 30 severe wind-producing MCSs occurring over the three year period: one in the Ohio River Valley in Kentucky and another in southwestern Georgia. There is also a relative maximum in eastern Pennsylvania. The prevalence of severe wind-producing MCSs decreases towards the western Great Plains. The reason is likely twofold: population is lower in the western Great Plains, so there are fewer possibilities for severe winds to be reported, and there are fewer trees and structures to be damaged, so there are fewer instances of wind damage.

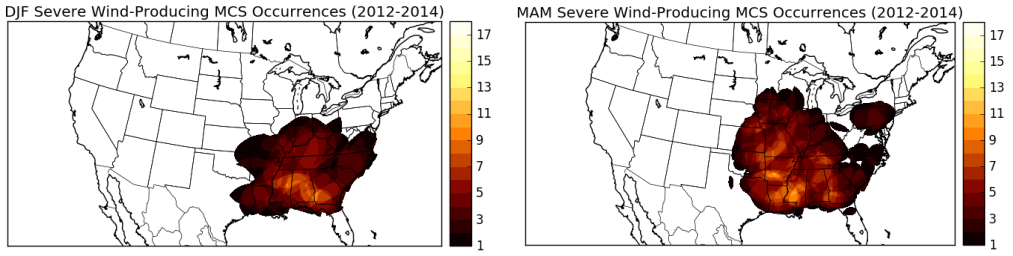

(a) December, January, and February

(b) March, April, and May

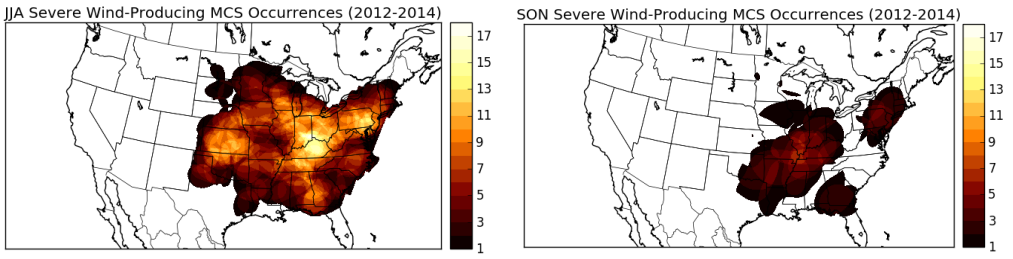

(c) June, July, and August

(d) September, October, and November

Figure 3.7: As in Figure 3.6, broken down by season.

In Figure 3.7, the full-year climatology is broken down by seasons. The most activity occurs in the summer (June, July, and August, Figure 3.7c), followed by the spring (March, April, and May, Figure 3.7b). The fewest number of events occur in the fall (September, October, and November, Figure 3.7d) and winter (December, January, and February, Figure 3.7a). The maximum in Kentucky that was seen in the full-year climatology can also be seen in the summer climatology. Generally, the maximum moves to the north in the warm season and back to the south in the cool season.

The number of severe wind-producing MCSs expected per day are shown in Figure 3.8. As would be expected due to the seasonal climatologies showing more severe wind-producing MCSs in the summer, the maximum occurs in the summer. The 31 day window has an absolute maximum on 13 June, when 0.70 severe wind-producing MCSs occurred per day. The 91 day window has an absolute maximum on 14 June, when 0.48 severe wind-producing MCSs occurred per day. There are several relative maxima with the 31 day window, though none are apparent in

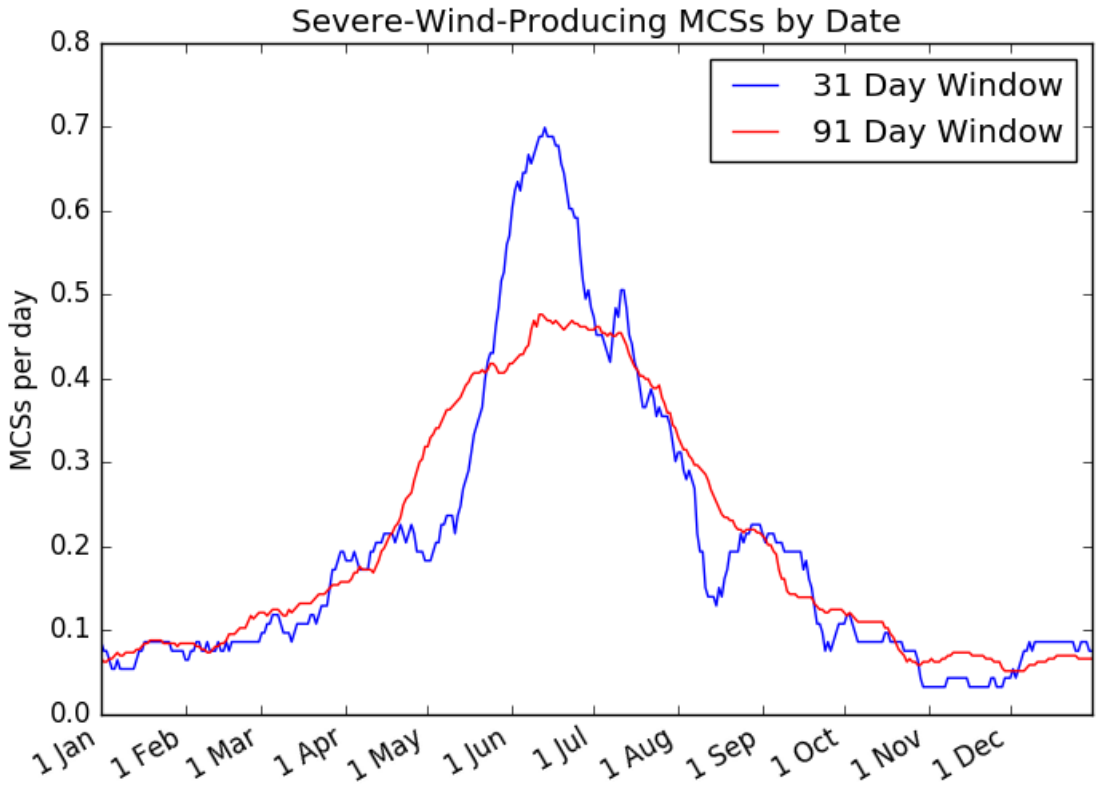

Figure 3.8: Running mean of severe wind-producing MCSs by date.

the 91 day window. This matches Smith et al. (2013), which found that wind gusts associated with QLCSs occurred most often in June. Derechos occur most frequently in May (Bentley and Sparks, 2003). Jirak et al. (2003) found that MCSs in general (not restricted to severe wind-producing MCSs) have a maximum in July, but that May and June also have a large number of MCSs. This suggests that a change occurs between May and June that results in more severe wind-producing MCSs, but no major change in the number of MCSs, though more research would be needed to determine what causes the change.

Chapter 4

Verification of 10 m Winds from NSSL-WRF for Severe Wind Events

4.1 Results of Verification

NSSL-WRF 10 m wind forecasts will be verified using three methods: traditional grid-point verification, grid-based verification using MODE, and object-based verification using MODE.

4.1.1 Traditional Grid-Point Verification

Verification was initially attempted by counting hits if 10 m winds above a threshold were forecast in the same 4-km grid square as a severe wind report with no smoothing on either field. False alarms were counted if forecast 10 m winds above a threshold were forecast in a grid square that had no severe wind reports. Misses were counted if forecast 10 m winds were below the threshold in a grid square that had a severe wind report. As can be seen from Figure 4.1, verification using this method provides no useful insight since the false alarm rate for all forecast thresholds is near 1. This mirrors what was found in Sobash et al. (2011). Using this method, critical success index is near 0 for all forecast thresholds. Since little to

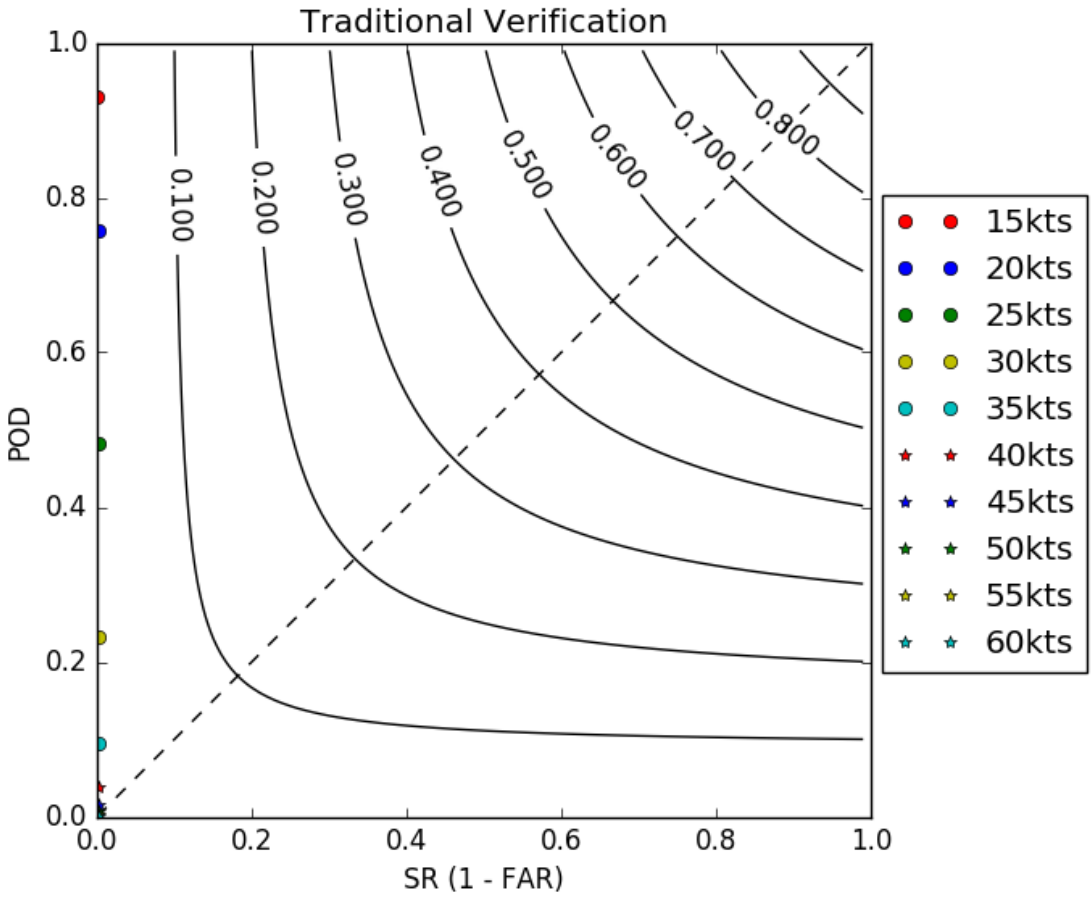

Figure 4.1: Traditional grid-point verification with no smoothing in either forecast or observation fields for NSSL-WRF forecasts of 10 m winds compared to unfiltered local storm reports from 2012 - 2014.

no information can be gleaned from traditional grid-point verification, verification using MODE will be done in this study.

4.1.2 Grid-based Verification using MODE

The same 25% convolution and 3000 grid square minimum area thresholds that best identified observed objects were also used to identify forecast objects. When using MODE and considering a grid-based verification, CSI is below 0.10 for all forecast thresholds (Figure 4.2). The maximum CSI of 0.075 occurs at a forecast

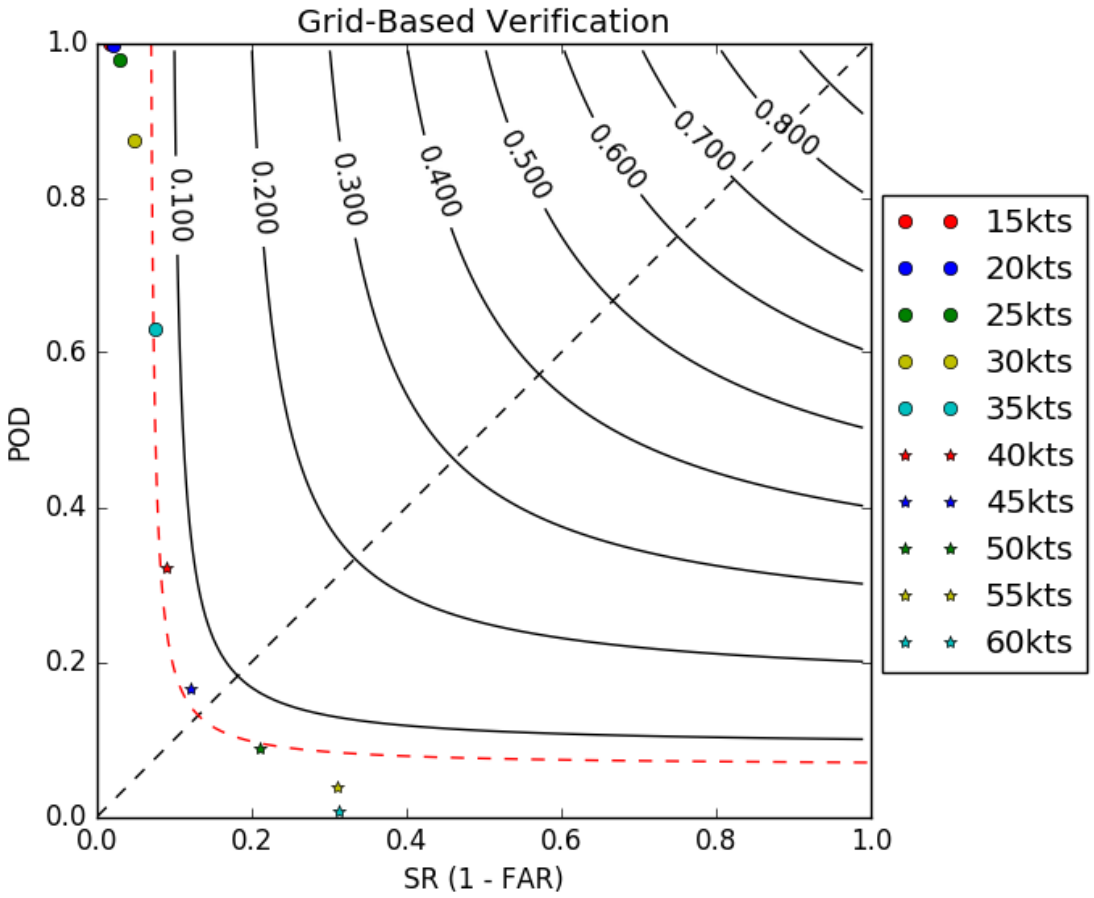

Figure 4.2: As in Figure 4.1, except for grid-based verification of various forecast thresholds using MODE. The 0.070 CSI contour is highlighted.

threshold of 45 kts. For forecast thresholds between 30 kts and 50 kts, the CSI stays relatively close to 0.070 (highlighted in the figure). For low thresholds, the forecast approaches "always yes." That is, forecast objects cover nearly the entire domain for every forecast. As the forecast threshold increases, POD decreases dramatically, while FAR only decreases slightly. At the 45 kt threshold, the bias is near 1, and as the forecast threshold increases above 45 kts, POD still decreases, though less dramatically and FAR starts to decrease more rapidly. For the highest threshold, 60 kts, POD is near 0.

4.1.3 Object-based Verification using MODE

When considering object-based verification (Figure 4.3), the general trend is similar to that observed in the M ODE grid-based verification, though CSI is higher for object-based verification. The maximum CSI of 0.16 occurs at a forecast threshold of 50 kts, which is the severe wind threshold set by the NWS. The 50 kt forecast threshold also produces the bias nearest to 1. Between the 35 kt and 50 kt thresholds, CSI stays very close to 0.15 (highlighted in the figure). As was seen with grid-based verification, forecasts are very low thresholds approach "always yes," though there is a lower FAR for object-based verification than for grid-based. For the 3 lowest thresholds, POD is equal to 1. As the forecast threshold increases, POD decreases dramatically, and FAR decreases slightly until the 45 kt threshold. For thresholds above 45 kts, FAR decreases nearly as fast as POD. As in grid-based verification, the highest threshold, 60 kts, has a POD near 0. The dramatic decrease in POD without much decrease in FAR for thresholds between 35 kts and 45 kts suggests that 35 kts may be a more useful threshold to forecasters. The slight decrease in FAR may not be worth the dramatic decrease in POD when using a higher threshold. If the costs of a missed event are greater than the costs of a false alarm, then choosing a lower threshold may be worth it.

4.2 Case Studies

To help better understand how MODE verifies NSSL-WRF forecasts, two cases will be examined. Each is one of 13 days on which a 60 kt forecast object was identified. In the first case, 24 July 2014, the forecast object went unmatched. In the second case, 14 June 2014, the forecast object was matched to an observation object.

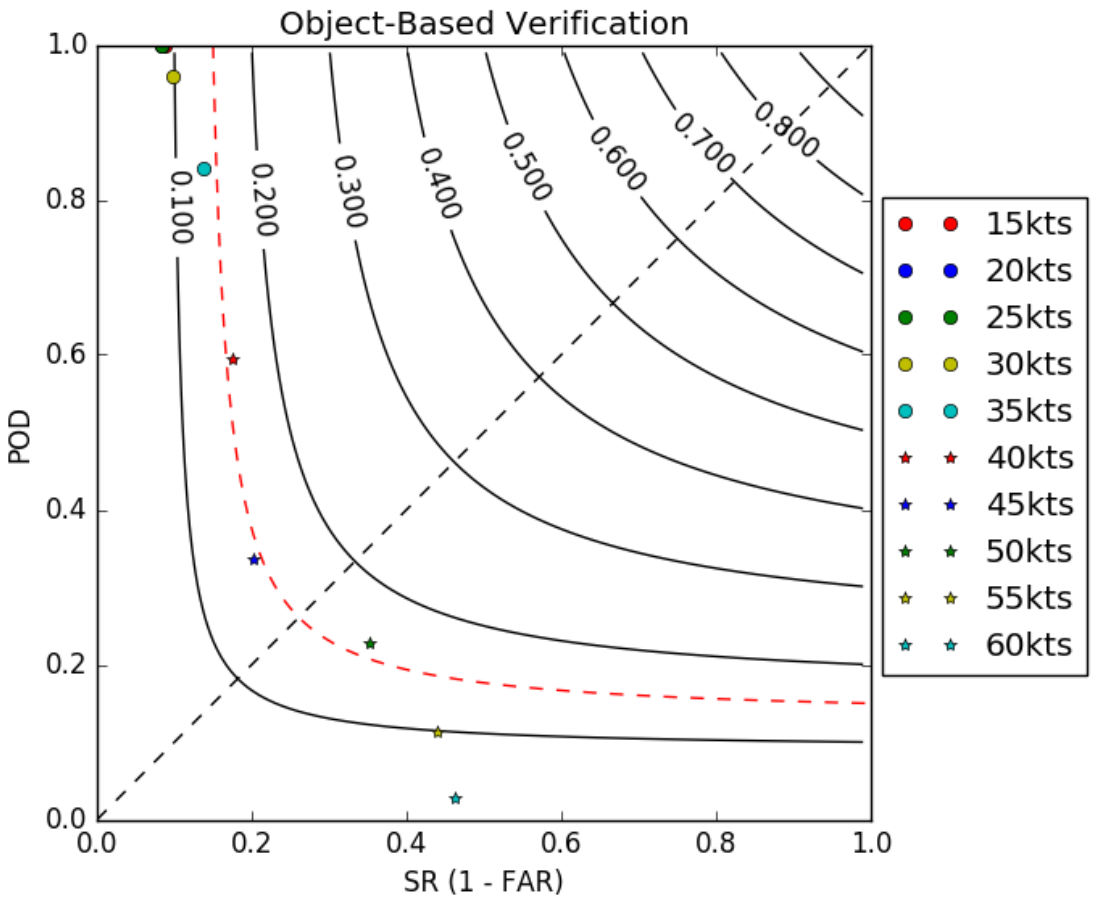

Figure 4.3: As in Figure 4.1, except for object-based verification of various forecast thresholds using MODE. The 0.15 CSI contour is highlighted.

4.2.1 24 July 2014

There were 7 days on which a 60 kt forecast was not matched with an observed severe wind-producing MCS. One of the unmatched forecasts occurred on 24 July 2014, which was chosen for further analysis. There were two events to note on 24 July, one in the northern Great Plains and one in the Mid-Atlantic.

In the northern Great Plains, several thunderstorms formed near the Canadian border by 2155Z (as indicated on radar in Figure 4.4a). The first reports associated with these storms came in at 2215Z in Phillips County, Montana. The storms moved into an area with 100mb MLCAPE of more than 3000 J kg^{-1}, according to the mesoanalysis available from Carbin et al. (2016). By 2355Z, the storms had coalesced into a line (Figure 4.4b), though the area of contiguous reflectivity above 35dBZ remained below 500 grid squares (8000 km^2) so all reports associated with this event were filtered out of the local storm wind reports. This event was more of a discrete convective mode, with most of the wind reports coming from supercells, compared to a more organized leading-line/trailing-stratiform MCS. In that regard, the radar filtering worked as intended even though there was a cluster of severe wind reports.

In the Mid-Atlantic, thunderstorms from the previous convective day were still active and producing severe wind reports at 12Z. By 1255Z, the storms were beginning to move off the coast (Figure 4.5a) and had ceased to produce severe wind reports. New storms formed by 1955Z (Figure 4.5b) and the first severe wind associated with the new convection was reported at 2014Z in Amelia County, Virginia. By 2155Z (Figure 4.5c), the storms had coalesced into a line and continued to produce severe wind reports. The final wind report was received at 2355Z in Randolph County, NC, and by then, the storm had nearly moved off the coast (Figure 4.5d).

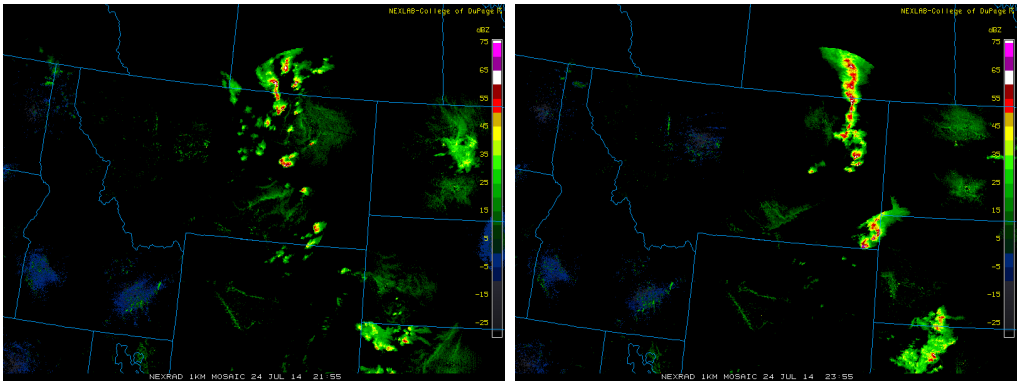

(a) 2255Z (b) 2355Z

Figure 4.4: Composite radar reflectivity for the 24 July 2014 convective day in the northern Plains. The domain is from roughly the center of the Dakotas in the east to the Idaho-Washington border in the west, and from about 300 km into Canada in the north to the Wyoming-Utah border in the south.

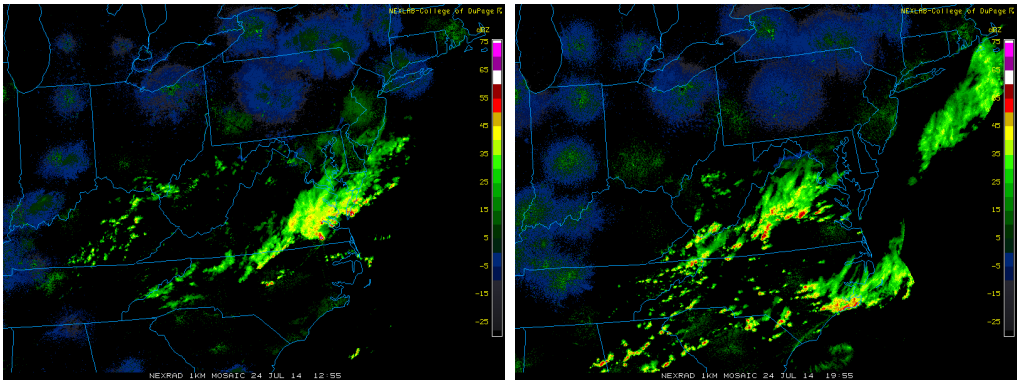

(a) 1255Z (b) 1955Z

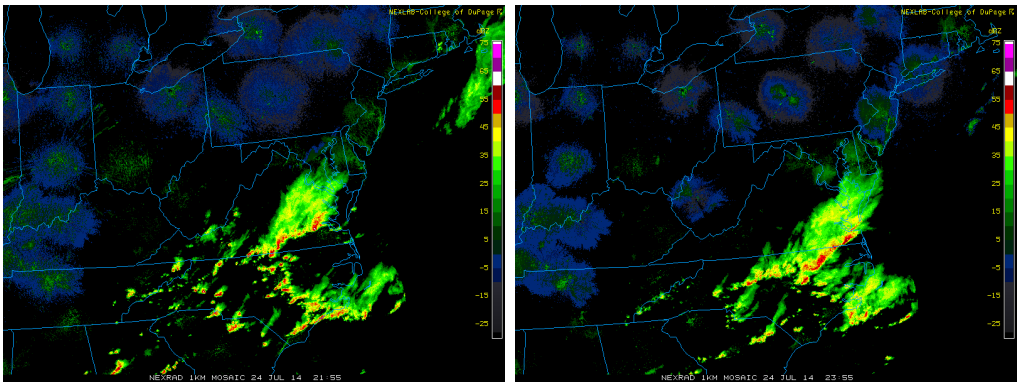

(c) 2155Z (d) 2355Z

Figure 4.5: Composite radar reflectivity for the 24 July 2014 convective day.

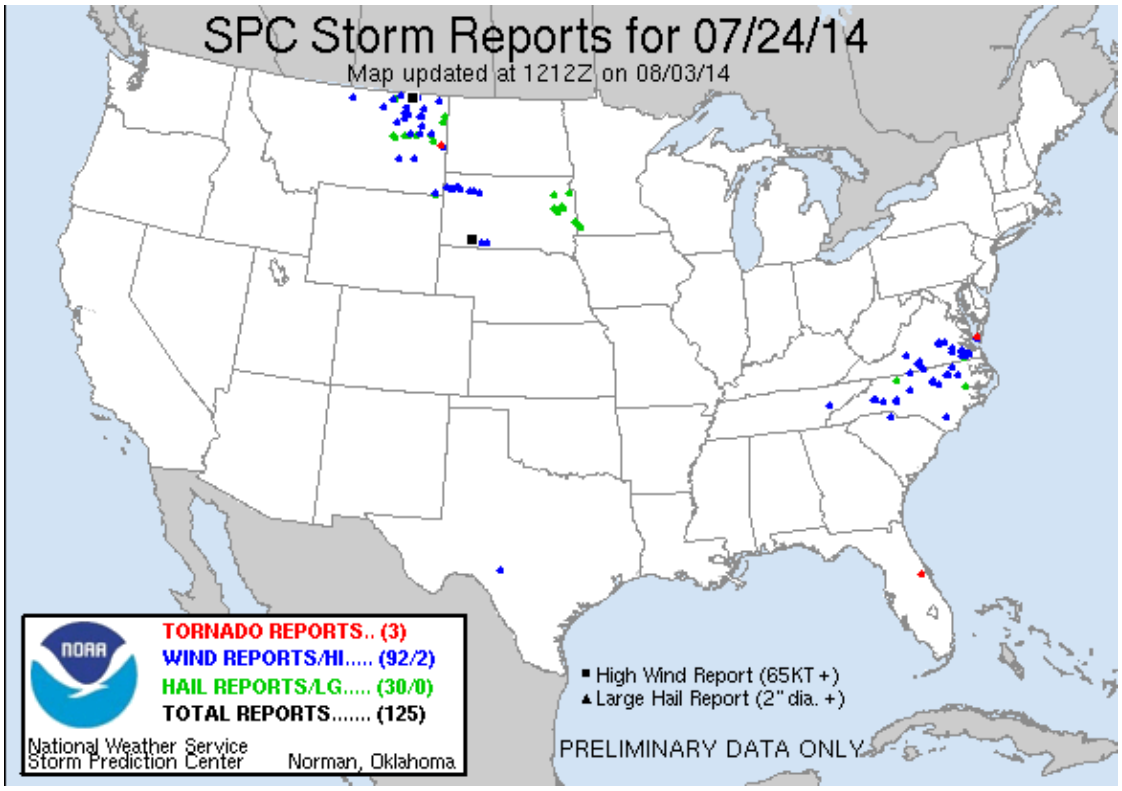

Figure 4.6: All local storm reports for the 24 July 2014 convective day. Wind reports are blue dots, and significant wind reports are black squares.

The practically perfect smoothed radar-filtered local storm reports (Figure 4.7) identify a single object in the Mid Atlantic associated with the convection in the area. The wind reports received in the northern Great Plains (Figure 4.6) were all excluded because radar reflectivity did not meet MCS criteria in the area.

The NSSL-WRF was forecast strong winds in the northern Great Plains, with forecast 10 m winds above 60 kts (Figure 4.8). In the Mid Atlantic, most the strongest NSSL-WRF winds were off of the coast. The practically perfect smoothed forecast (Figure 4.9) shows false alarms for the northern Great Plains in all forecast thresholds. Winds only appear in the Mid Atlantic for the 30 kt and 40 kt thresholds. The objects identified by MODE in both the forecast and observations are shown in Figure 4.10. The "false alarm" in the northern Great Plains can be

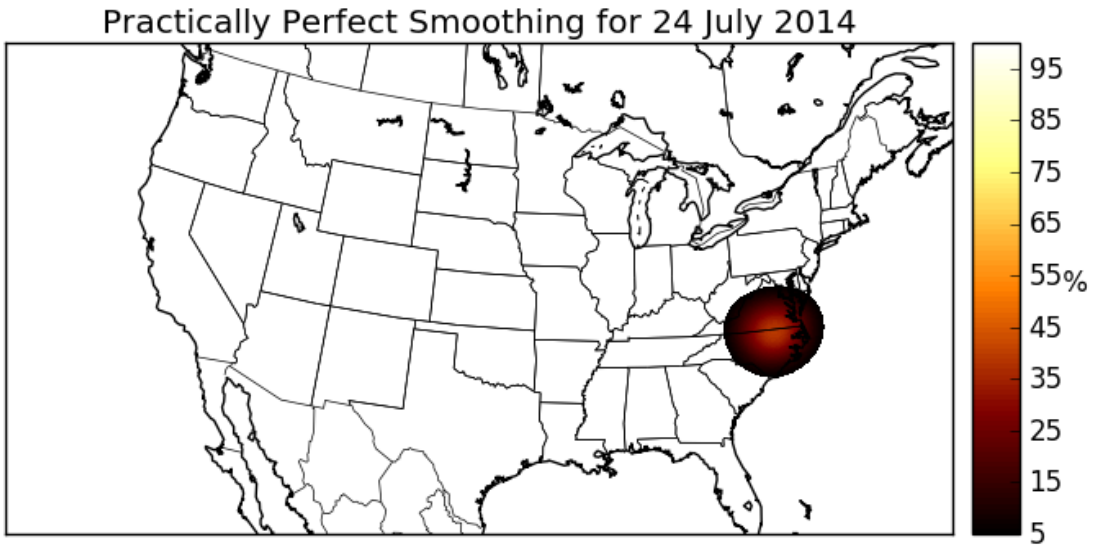

Figure 4.7: Practically perfect smoothed radar filtered local storm reports for 24 July 2014.

seen in all forecast thresholds. The only forecast object that matched with the observed object was at the 30 kt threshold, with an interest score 0.902. Across all four thresholds, there are examples of hits (the matched objects at 30 kts), misses (the unmatched observation object at thresholds above 30 kt), and false alarms (objects in the northern Great Plains at all forecast thresholds). Though it resulted in a forecast miss, the radar filtering of storm reports works as intended here. The radar filtering is employed to eliminate wind reports not associated with an organized MCS, and it does so here, since the storms in the northern plains remained discrete until late, and most reports were associated with the discrete storms.

4.2.2 14 June 2014

In addition to the 7 unmatched 60 kt objects, there were 6 days on which a 60 kt forecast matched with an observed severe wind-producing MCS, and 14 June 2014 was chosen for further analysis. By 2255Z on 14 June (Figure 4.11a), storms

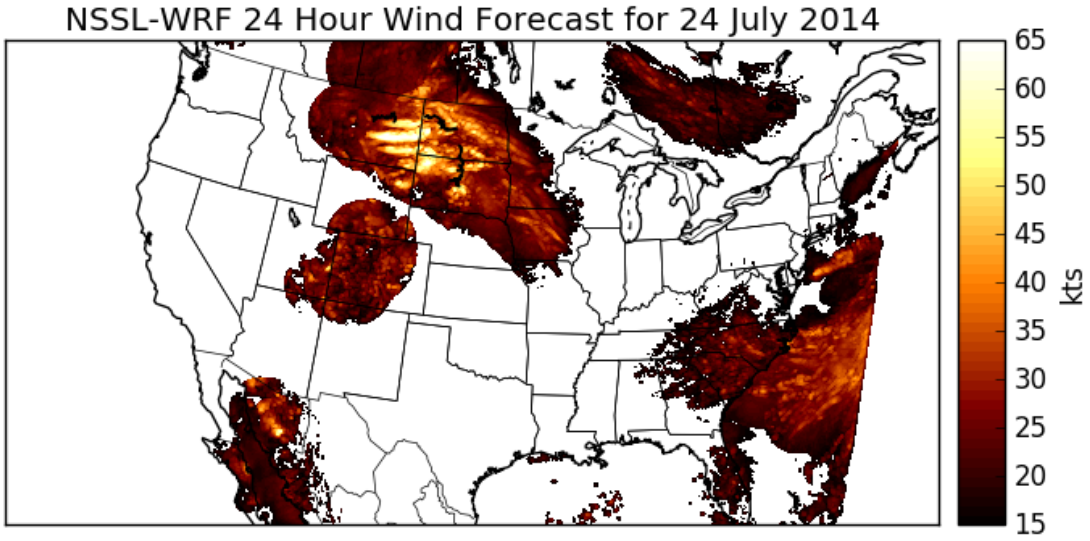

Figure 4.8: NSSL-WRF 10 m 24 hour maximum wind field for 24 July 2014.

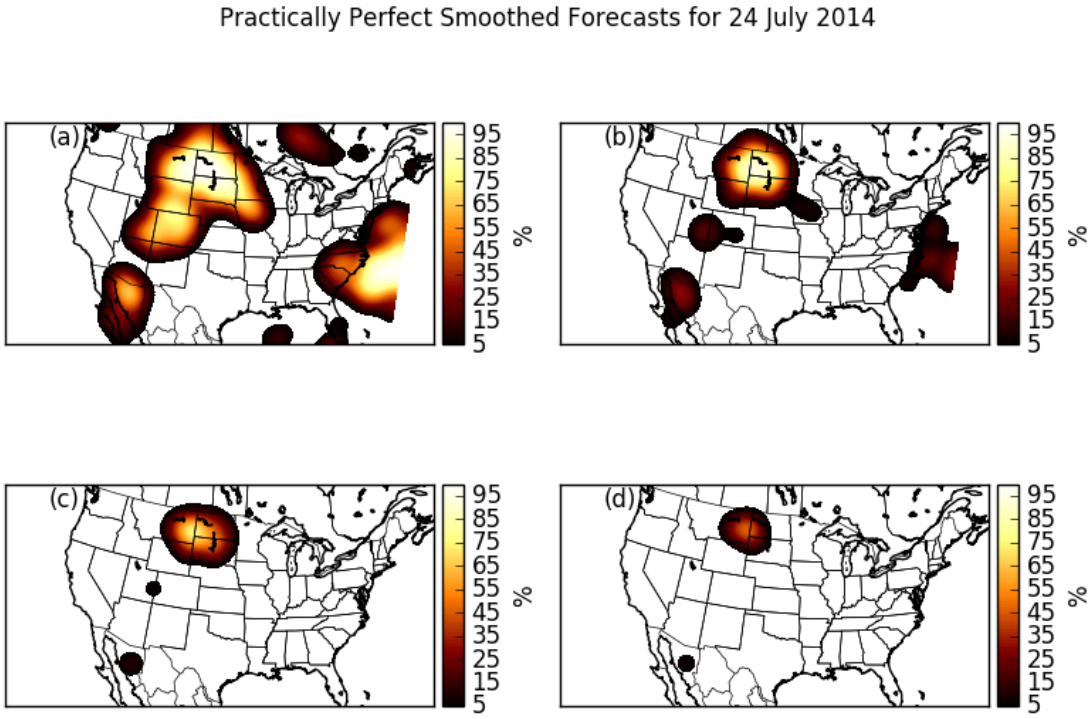

Figure 4.9: Pracitcally perfect smoothed forecasts for (a) 30 kt, (b) 40 kt, (c) 50 kt, and (d) 60 kt forecast thresholds for 24 July 2014 based on the forecast shown in Figure 4.8.

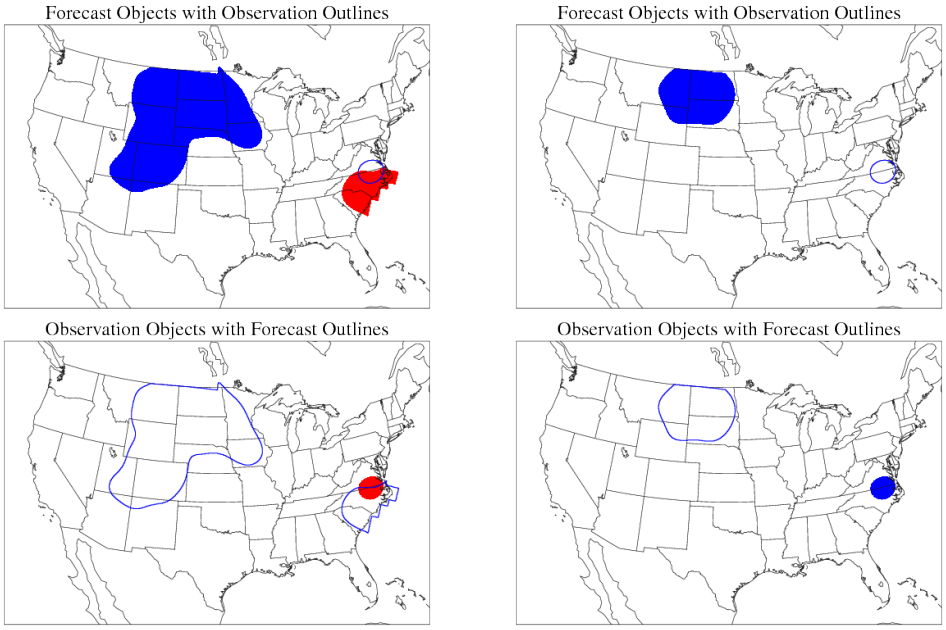

(a) 30 kts

(b) 40 kts

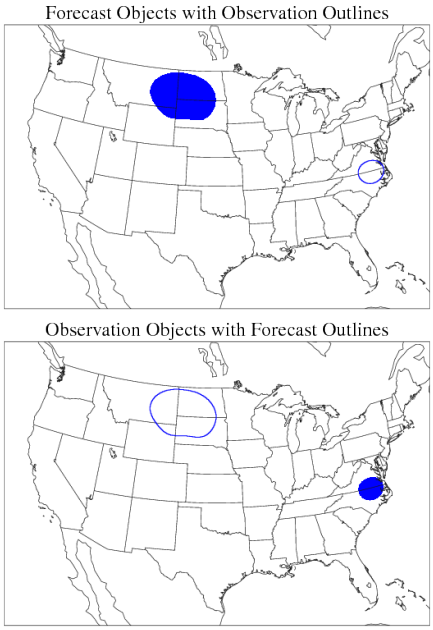

(c) 50 kts

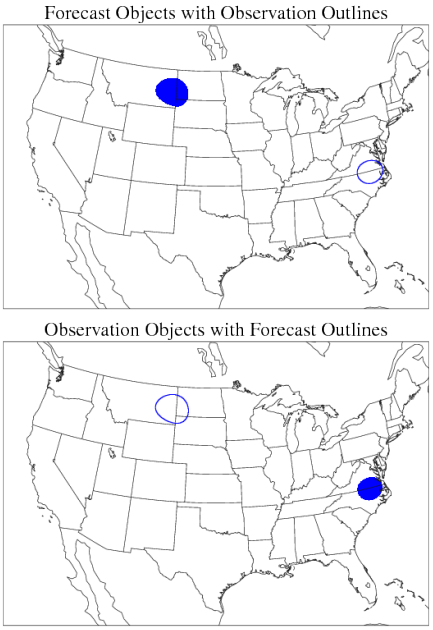

(d) 60 kts

Figure 4.10: MODE-identified objects for 24 July 2014. The top panel of each subfigure shows forecast objects filled with observed objects outlined. The bottom panel shows the opposite: observed objects filled with forecast objects outlined. Red fill indicated that the object was matched, while blue fill indicates an unmatched object.

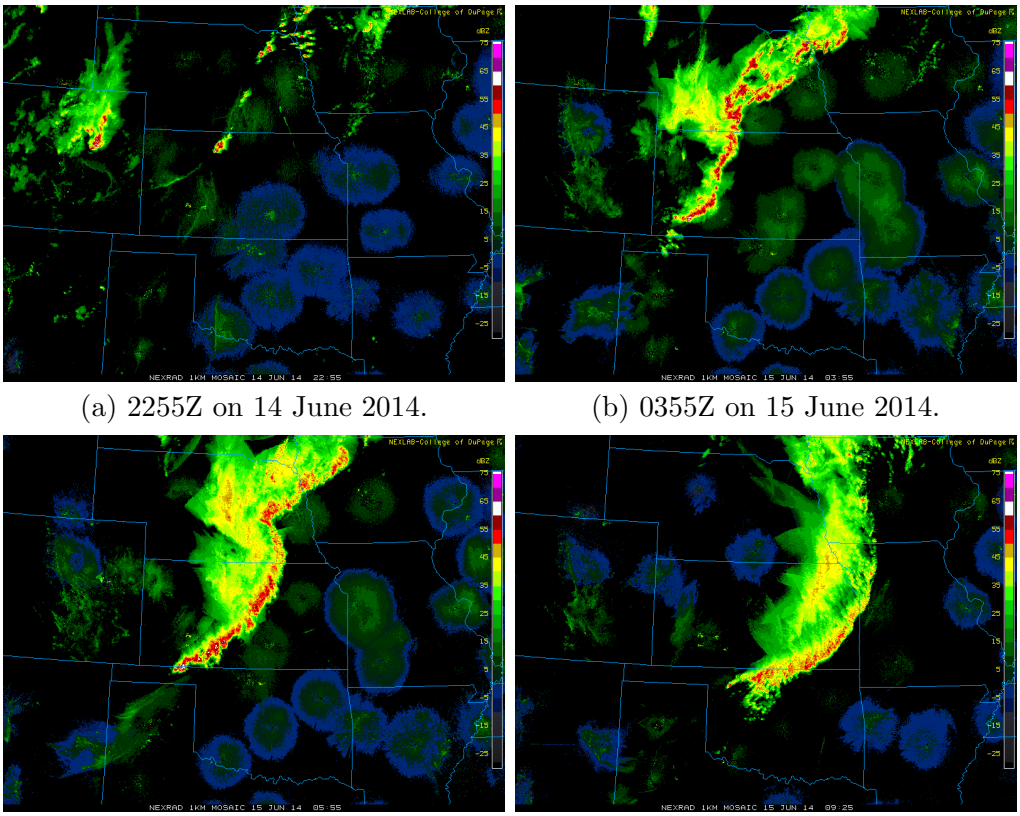

(a) 2255Z on 14 June 2014.

(b) 0355Z on 15 June 2014.

(c) 0555Z on 15 June 2014.

(d) 0925Z on 15 June 2014.

Figure 4.11: Composite radar reflectivity for the 14 June 2014 convective day.

had initiated near Denver, CO and began to move to the east into an area with 100 millibar mixed layer convective available potential energy (100mb MLCAPE) of 3000 Jkg^{-1} according the mesoanalysis available at Carbin et al. (2016). The first wind report was received at 2350Z in Kit Carson County, CO with estimated gusts between 60 and 70mph (52-61kts, 27-31ms^{-1}). By 0355Z (Figure 4.11b), the storms had merged with other storms in southern Nebraska and organized into a quasi-linear convective system (QLCS), centered on the Kansas-Nebraska border. By 0555Z (Figure 4.11c), the QLCS had evolved further into a bow echo with its apex along the Kansas-Nebraska border. The final wind report was received at 0923Z on 15 June 2014 in Lee's Summit County, MO and by 0925Z (Figure 4.11d) the radar structure had nearly completely decayed.

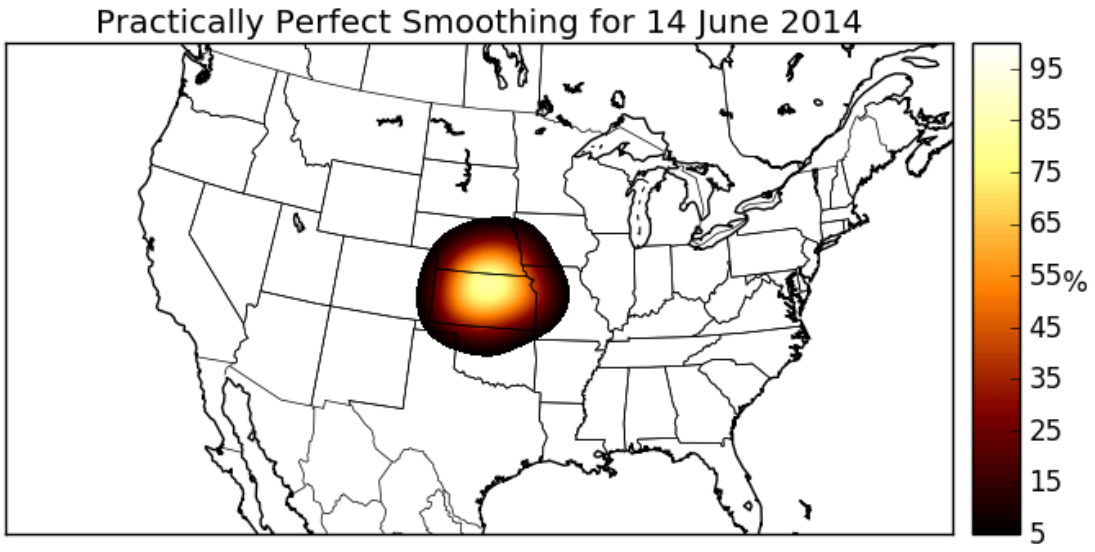

Figure 4.12: Practically perfect smoothed local storm reports filtered by radar reflectivity for 14 June 2014.

The practically perfect smoothed local storm reports, when filtered by radar reflectivity (Figure 4.12), identify a single object centered over northern Kansas associated with the QLCS seen in radar reflectivity. Though not counted separately when verifying, significant wind reports accounted for 31 of the 235 wind reports received for the day (Figure 4.13). The majority of the significant wind reports were associated with the severe wind-producing MCS.

The NSSL-WRF winds appeared to be in roughly the same area as the storm reports, though there were some spurious winds in the panhandles of Texas and Oklahoma that were not seen in the local storm reports (Figure 4.14). The practically perfect smoothed forecasts (Figure 4.15) show that the model forecasts too broad of an area of winds below 50 kts, but the 50 kt and 60 kt forecasts appear to cover mostly the correct area, though the probability magnitudes are far lower than for the observations. The objects identified by MODE in both the forecast and observations are shown in Figure 4.16. Subjectively, it appears that the 50 kt forecast did best, with the 60 kt forecast underforecasting, and the other forecasts

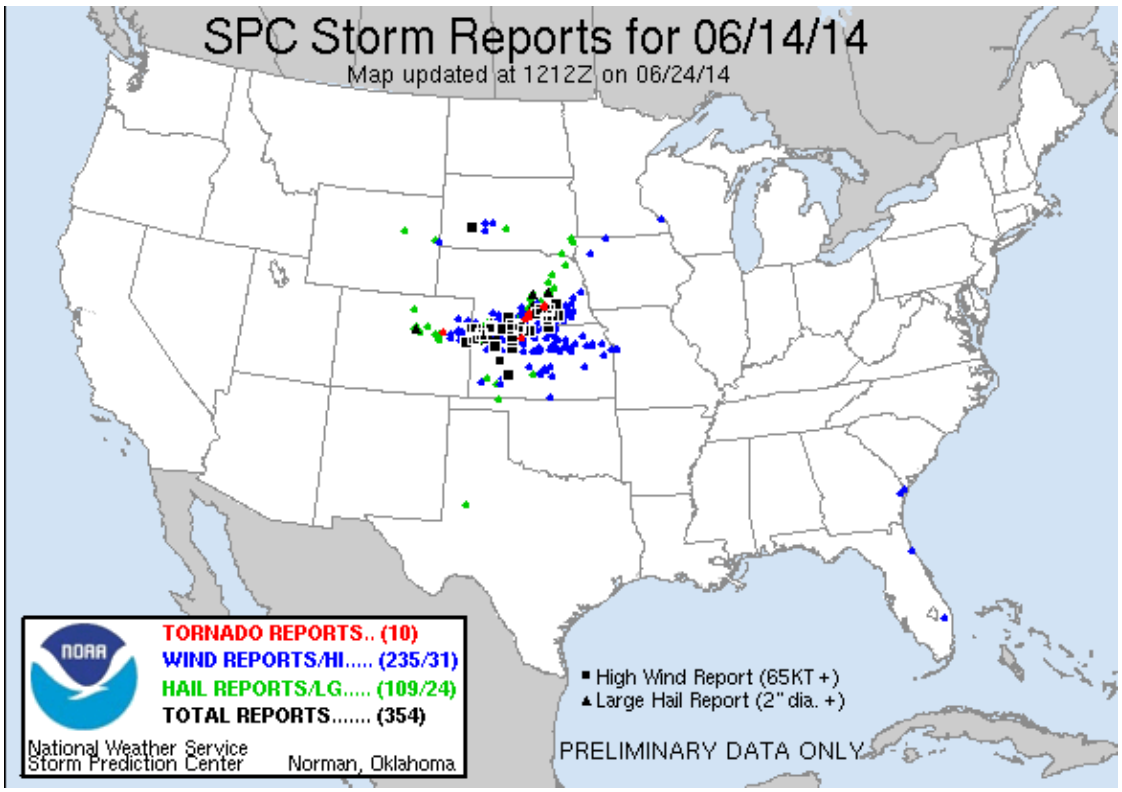

Figure 4.13: All local storm reports for the 14 June 2014 convective day. Wind reports are blue dots, and significant reports are black squares.

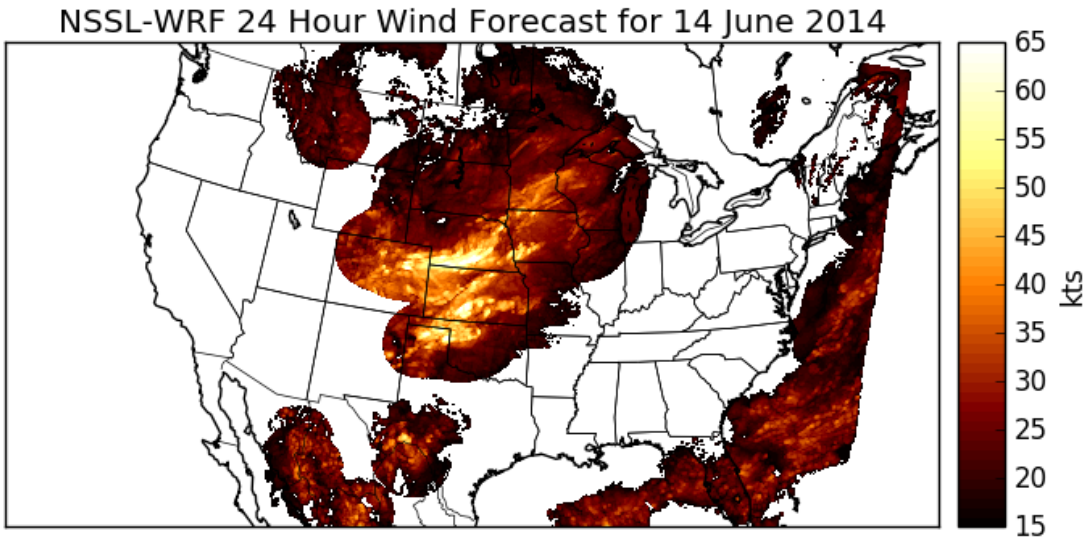

Figure 4.14: NSSL-WRF 10 m 24 hour maximum filtered by simulated reflectivity wind field for 14 June 2014.

overforecasting, particularly the 30 kt forecast, which had two additional forecast objects. The interest scores for the four thresholds presented (from lowest threshold to highest) are: 0.8889, 0.9128, 0.9481, and 0.8817. If interest scores are taken as a measure of forecast quality, the 50 kt forecast did best.

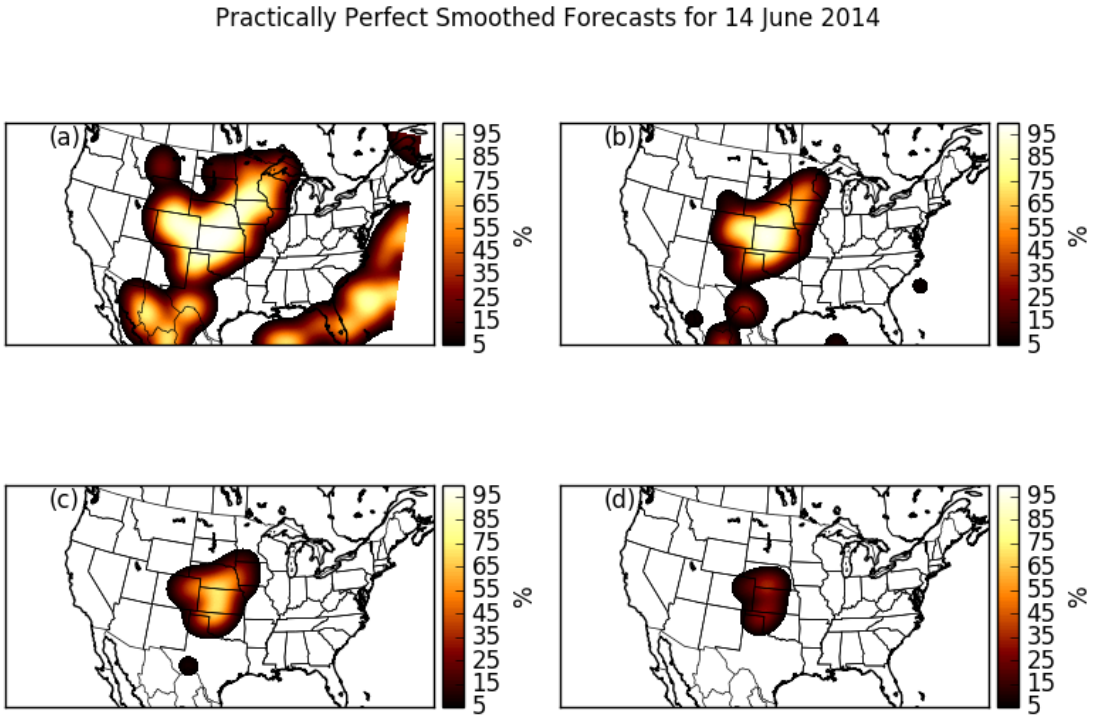

Figure 4.15: Practically perfect smoothed forecasts for (a) 30 kt, (b) 40 kt, (c) 50 kt, and (d) 60 kt thresholds for 14 June 2014 based on the forecast shown in Figure 4.14.

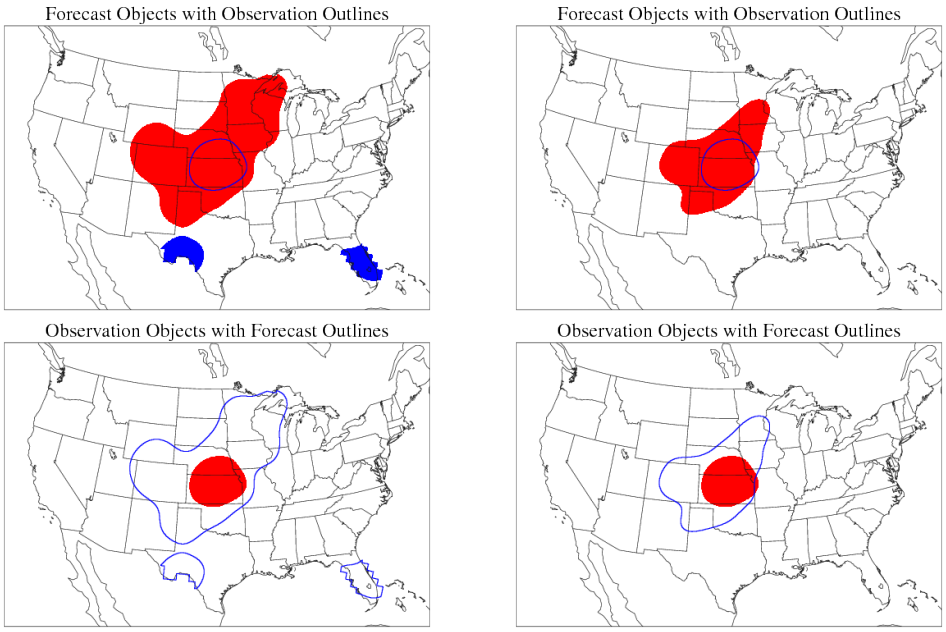

(a) 30 kts

(b) 40 kts

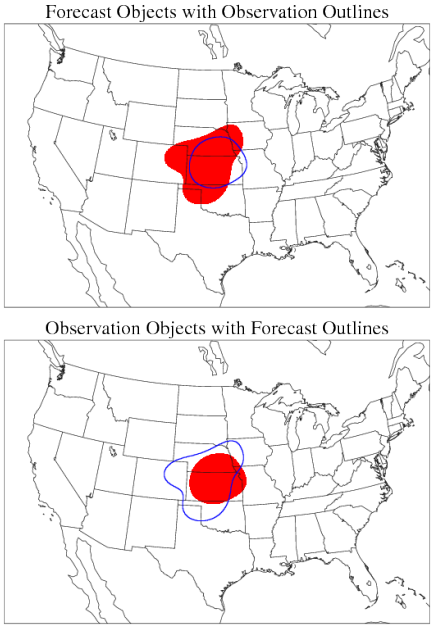

(c) 50 kts

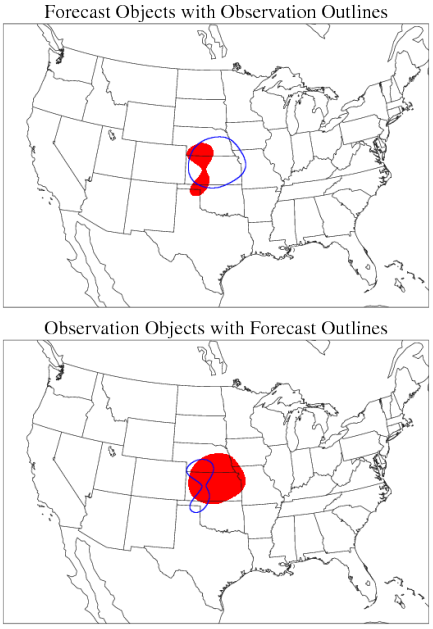

(d) 60 kts

Figure 4.16: MODE-identified objects for 14 June 2014.

Chapter 5

Conclusions

A climatology of severe wind-producing MCSs in 2012 - 2014 was developed using an object-based approach to identify severe wind-producing MCSs using severe wind reports and observed radar reflectivity. To develop the climatology, MODE was used to identify severe wind objects that were based on a practically perfect hindcast of severe wind reports filtered by radar reflectivity. MODE identifies objects using user-defined intensity and minimum area thresholds, then matches forecast and observation objects using a fuzzy logic engine. Severe wind-producing MCSs occurred most often in the Ohio River Valley, with a secondary maximum in southwestern Georgia and southeastern Alabama. Temporally, severe wind-producing MCSs occurred most often in the warm season with a peak in June. This climatology is generally consistent with other climatologies of severe wind reports and MCSs (e.g., Gallus et al., 2008; Burke and Schultz, 2004; Smith et al., 2013).

To verify the NSSL-WRF, a 24-hour maximum 10 m wind field was generated from forecast hours 12 - 36 of the 0000 UTC model run and filtered by simulated reflectivity using the same parameters as were used to filter the wind reports. Thresholds between 15 kt and 60 kt were examined in the forecast field, then the forecast field was smoothed using the same parameters that were applied to create the hindcast of the severe wind reports. MODE was again used to identify forecast

objects that were matched to observed objects using a fuzzy logic engine. Verification metrics were computed several ways: traditional grid-point verification, grid-based verification using MODE, and object-based verification using MODE. Traditional grid-point verification provided little useful insight, but it justified the use of an object-based approach to verify the forecast. Grid-based and object-based verification using MODE both showed that the model had a relatively constant critical success index across a range of forecast wind speed thresholds. Object-based verification using MODE yielded higher values of CSI than grid-based verification using MODE. Additionally, though wind-speed forecasts at higher thresholds yielded biases nearest to one and the highest CSIs, wind-speed forecasts at lower thresholds with slightly lower CSIs might be more useful for forecasters since POD is dramatically higher at lower thresholds without a large penalty in FAR. Using a lower forecast wind-speed threshold captures more events (e.g. a 50 kt threshold captures fewer events than a 35 kt threshold), and most of the additional events captured are matched to an observed object.

When considering severe wind-producing MCSs, the NSSL-WRF overforecasts at low wind speed thresholds and underforecasts at higher wind speed thresholds. By filtering the model winds with simulated radar reflectivity, it was hoped that model performance for MCSs would be maximized. Even though object-based verification of severe MCS winds, as highlighted by the utility of CAM forecasts over traditional grid-point verification approaches, there may room for developing improved severe wind proxies from CAMs. Further research investigating fields in addition to 10 m winds as potential severe wind proxies is ongoing. This work provides baseline verification metrics for any potential new proxy. That is, a new proxy would have to generate better verification scores than 10-meter wind forecasts to show utility in forecasting severe wind-producing MCSs.

Bibliography

Ahijevych, D., E. Gilleland, B. G. Brown, and E. E. Ebert, 2009: Application of Spatial Verification Methods to Idealized and NWP-Gridded Precipitation Forecasts. *Weather and Forecasting*, **24 (6)**, 1485–1497, doi:10.1175/2009WAF2222298.1, URL http://journals.ametsoc.org/doi/abs/10.1175/2009WAF2222298.1.

Beck, J., M. Nuret, and O. Bousquet, 2014: Model Wind Field Forecast Verification Using Multiple-Doppler Syntheses from a National Radar Network. *Weather and Forecasting*, **29 (2)**, 331–348, doi:10.1175/WAF-D-13-00068.1, URL http://journals.ametsoc.org/doi/abs/10.1175/WAF-D-13-00068.1.

Bentley, M. L., and J. a. Sparks, 2003: A 15 yr climatology of derecho-producing mesoscale convective systems over the central and eastern United States. *Climate Res.*, **24**, 129–139, doi:10.3354/cr024129, URL http://www.ottokinne.de/articles/cr2003/24/c024p129.pdf.

Brooks, H., 2013: Severe thunderstorms and climate change. *Atmospheric Research*, **123**, 129–138, doi:10.1016/j.atmosres.2012.04.002.

Brown, B. G., L. Holland, J. E. H. Gotway, R. Bullock, D. A. Ahijevych, E. Gilleland, and C. A. Davis, 2007: Application of the MODE object-based verification tool for the evaluation of model precipitation fields. *22nd Conference on Weather Analysis and Forecasting / 18th Conference on Numerical Weather Prediction*, 8, URL https://ams.confex.com/ams/22WAF18NWP.

Burke, P. C., and D. M. Schultz, 2004: A 4-Yr Climatology of Cold-Season Bow Echoes over the Continental United States. *Weather and Forecasting*, **19**, 1061–1074, doi:10.1175/811.1.

Carbin, G., and Coauthors, 2016: Storm Prediction Center Storm Severe Weather Summary Page. NOAA's National Weather Service, URL http://www.spc.noaa.gov/exper/archive/events/.

Chen, F., and J. Dudhia, 2001: Coupling an Advanced Land Surface–Hydrology Model with the Penn State–NCAR MM5 Modeling System. Part I: Model Implementation and Sensitivity. *Monthly Weather Review*, **129 (4)**, 569–585, doi:10.1175/1520-0493(2001)129⟨0569:CAALSH⟩2.0.CO;2.

Clark, A. J., R. G. Bullock, T. L. Jensen, M. Xue, and F. Kong, 2014: Application of object-based time-domain diagnostics for tracking precipitation systems in convection-allowing models. *Weather and Forecasting*, 140117143410005, doi:10.1175/WAF-D-13-00098.1.

Cohen, A. E., M. C. Coniglio, S. F. Corfidi, and S. J. Corfidi, 2007: Discrimination of Mesoscale Convective System Environments Using Sounding Observations. *Weather and Forecasting*, **22 (5)**, 1045–1062, doi:10.1175/WAF1040.1, URL http://journals.ametsoc.org/doi/abs/10.1175/WAF1040.1.

Coniglio, M. C., H. E. Brooks, S. J. Weiss, and S. F. Corfidi, 2007: Forecasting the Maintenance of Quasi-Linear Mesoscale Convective Systems. *Weather and Forecasting*, **22 (3)**, 556–570, doi:10.1175/WAF1006.1.

Corfidi, S. F., M. C. Coniglio, A. E. Cohen, and C. M. Mead, 2016: A Proposed Revision to the Definition of "Derecho". *Bulletin of the American Meteorological Society*, **97 (6)**, 935–949, doi:10.1175/BAMS-D-14-00254.1, URL http://journals.ametsoc.org/doi/10.1175/BAMS-D-14-00254.1.

Davis, C., B. Brown, and R. Bullock, 2006: Object-Based Verification of Precipitation Forecasts. Part I: Methodology and Application to Mesoscale Rain Areas. *Monthly Weather Review*, **134 (7)**, 1772–1784, doi:10.1175/MWR3145.1.

Done, J., C. A. Davis, and M. Weisman, 2004: The next generation of NWP: explicit forecasts of convection using the weather research and forecasting (WRF) model. *Atmospheric Science Letters*, **5 (6)**, 110–117, doi:10.1002/asl.72, URL http://doi.wiley.com/10.1002/asl.72.

Doswell, C. A., H. E. Brooks, and M. P. Kay, 2005: Climatological Estimates of Daily Local Nontornadic Severe Thunderstorm Probability for the United States. *Weather and Forecasting*, **20 (4)**, 577–595, doi:10.1175/WAF866.1, URL http://journals.ametsoc.org/doi/abs/10.1175/WAF866.1.

Doswell, C. A., and D. W. Burgess, 1988: On Some Issues of United States Tornado Climatology. *Monthly Weather Review*, **116 (2)**, 495–501, doi:10.1175/1520-0493(1988)116⟨0495:OSIOUS⟩2.0.CO;2.

Dudhia, J., 1989: Numerical Study of Convection Observed during the Winter Monsoon Experiment Using a Mesoscale Two-Dimensional Model. *Journal of the Atmospheric Sciences*, **46 (20)**, 3077–3107, doi:10.1175/1520-0469(1989)046⟨3077:NSOCOD⟩2.0.CO;2.

Gallus, W. A., N. A. Snook, and E. V. Johnson, 2008: Spring and Summer Severe Weather Reports over the Midwest as a Function of Convective Mode: A Preliminary Study. *Weather and Forecasting*, **23 (1)**, 101–113, doi:10.1175/2007WAF2006120.1, URL http://journals.ametsoc.org/doi/abs/10.1175/2007WAF2006120.1.

Hitchens, N. M., H. E. Brooks, and M. P. Kay, 2013: Objective Limits on Forecasting Skill of Rare Events. *Weather and Forecasting*, **28 (2)**, 525–534, doi:10.1175/WAF-D-12-00113.1, URL http://journals.ametsoc.org/doi/full/10.1175/WAF-D-12-00113.1.

Hong, S.-Y., and J.-O. J. Lim, 2006: The WRF Single-Moment 6-Class Microphysics Scheme (WSM6). *Journal of the Korean Meteorological Society*, **42 (2)**, 129–151.

Houze, R. A., 2004: Mesoscale convective systems. *Reviews of Geophysics*, **42 (4)**, RG4003, doi:10.1029/2004RG000150, URL http://doi.wiley.com/10.1029/2004RG000150.

Janjić, Z. I., 1990: The Step-Mountain Coordinate: Physical Package. *Monthly Weather Review*, **118 (7)**, 1429–1443, doi:10.1175/1520-0493(1990)118⟨1429:TSMCPP⟩2.0.CO;2.

Jirak, I. L., W. R. Cotton, and R. L. McAnelly, 2003: Satellite and Radar Survey of Mesoscale Convective System Development. *Monthly Weather Review*, **131 (10)**, 2428–2449, doi:10.1175/1520-0493(2003)131⟨2428:SARSOM⟩2.0.CO;2.

Johns, R. H., and W. D. Hirt, 1987: Derechos: Widespread Convectively Induced Windstorms. *Weather and Forecasting*, **2 (1)**, 32–49, doi:10.1175/1520-0434(1987)002⟨0032:DWCIW⟩2.0.CO;2.

Kain, J. S., and Coauthors, 2008: Some Practical Considerations Regarding Horizontal Resolution in the First Generation of Operational Convection-Allowing NWP. *Weather and Forecasting*, **23 (5)**, 931–952, URL http://journals.ametsoc.org/doi/abs/10.1175/WAF2007106.1.

Kelly, D. L., J. T. Schaefer, and C. A. Doswell, 1985: Climatology of Nontornadic Severe Thunderstorm Events in the United States. *Monthly Weather Review*, **113 (11)**, 1997–2014, doi:10.1175/1520-0493(1985)113⟨1997:CONSTE⟩2.0.CO;2.

Klimowski, B. A., 1994: Initiation and Development of Rear Inflow within the 28-29 June 1989 North Dakota Mesoconvective System. *Monthly Weather Review*, **122 (5)**, 765–779, doi:10.1175/1520-0493(1994)122⟨0765:IADORI⟩2.0.CO;2.

Mecikalski, J. R., and K. M. Bedka, 2006: Forecasting Convective Initiation by Monitoring the Evolution of Moving Cumulus in Daytime GOES Imagery. *Monthly Weather Review*, **134 (1)**, 49–78, doi:10.1175/MWR3062.1, URL http://journals.ametsoc.org/doi/abs/10.1175/MWR3062.1.

Mellor, G. L., and T. Yamada, 1982: Development of a turbulence closure model for geophysical fluid problems. *Reviews of Geophysics*, **20 (4)**, 851, doi:10.1029/RG020i004p00851, URL http://doi.wiley.com/10.1029/RG020i004p00851.

Miller, D. J., and R. H. Johns, 2000: A Detailed Look at Extreme Wind Damage in Derecho Events. *20th Conference on Severe and Local Storms*, Orlando, FL, 52–55.

Mittermaier, M. P., and R. Bullock, 2013: Using MODE to explore the spatial and temporal characteristics of cloud cover forecasts from high-resolution NWP models. *Meteorological Applications*, **20 (2)**, 187–196, doi:10.1002/met.1393.

Mlawer, E. J., S. J. Taubman, P. D. Brown, M. J. Iacono, and S. A. Clough, 1997: Radiative transfer for inhomogeneous atmospheres: RRTM, a validated correlated-k model for the longwave. *Journal of Geophysical Research: Atmospheres*, **102 (D14)**, 16 663–16 682, doi:10.1029/97JD00237, URL http://doi.wiley.com/10.1029/97JD00237.

Parker, M. D., and R. H. Johnson, 2000: Organizational Modes of Midlatitude Mesoscale Convective Systems. *Monthly Weather Review*, **128 (10)**, 3413–3436, doi:10.1175/1520-0493(2001)129⟨3413:OMOMMC⟩2.0.CO;2.

Roebber, P. J., 2009: Visualizing Multiple Measures of Forecast Quality. *Weather and Forecasting*, **24 (2)**, 601–608, doi:10.1175/2008WAF2222159.1, URL http://journals.ametsoc.org/doi/abs/10.1175/2008WAF2222159.1.

Schmidt, J. M., and W. R. Cotton, 1990: Interactions between Upper and Lower Tropospheric Gravity Waves on Squall Line Structure and Maintenance. URL http://journals.ametsoc.org/doi/abs/10.1175/1520-0469(1990)047⟨1205:IBUALT⟩2.0.CO;2, 1205–1222 pp.

Skamarock, W. C., M. L. Weisman, and J. B. Klemp, 1994: Three-Dimensional Evolution of Simulated Long-Lived Squall Lines. *Journal of the Atmospheric Sciences*, **51 (17)**, 2563–2584, doi:10.1175/1520-0469(1994)051⟨2563:TDEOSL⟩2.0.CO;2, URL http://journals.ametsoc.org/doi/abs/10.1175/1520-0469(1994)051⟨2563:TDEOSL⟩2.0.CO;2.

Smith, B. T., T. E. Castellanos, A. C. Winters, C. M. Mead, A. R. Dean, and R. L. Thompson, 2013: Measured severe convective wind climatology and associated convective modes of thunderstorms in the contiguous United States, 2003-2009. *Weather and Forecasting*, **228**, 229–236, doi:10.1175/WAF-D-12-00096.1.

Sobash, R. A., J. S. Kain, D. R. Bright, A. R. Dean, M. C. Coniglio, and S. J. Weiss, 2011: Probabilistic Forecast Guidance for Severe Thunderstorms Based on the Identification of Extreme Phenomena in Convection-Allowing Model Forecasts. *Weather and Forecasting*, **26 (5)**, 714–728, doi:10.1175/WAF-D-10-05046.1, URL http://journals.ametsoc.org/doi/abs/10.1175/WAF-D-10-05046.1.

Trapp, R. J., D. M. Wheatley, N. T. Atkins, R. W. Przybylinski, and R. Wolf, 2006: Buyer Beware: Some Words of Caution on the Use of Severe Wind Reports in Postevent Assessment and Research. *Weather and Forecasting*, **21 (3)**,

408–415, doi:10.1175/WAF925.1, URL http://journals.ametsoc.org/doi/abs/10.1175/WAF925.1.

Van der Plas, E. V., B. Wichers Schreur, and K. Kok, 2012: A quantitative evaluation of the high resolution HARMONIE model for critical weather phenomena. *Advances in Science and Research*, **8**, 149–155, doi:10.5194/asr-8-149-2012, URL http://www.adv-sci-res.net/8/149/2012/.

Weisman, M. L., C. Davis, W. Wang, K. W. Manning, and J. B. Klemp, 2008: Experiences with 0–36-h Explicit Convective Forecasts with the WRF-ARW Model. *Weather and Forecasting*, **23 (3)**, 407–437, doi:10.1175/2007WAF2007005.1, URL http://journals.ametsoc.org/doi/abs/10.1175/2007WAF2007005.1.

Weiss, S., J. Hart, and P. Janish, 2002: An examination of severe thunderstorm wind report climatology: 1970–1999. *Preprints, 21st Conf. on Severe Local Storms, San ....*

Yang, M.-H., and R. A. Houze, 1995: Sensitivity of Squall-Line Rear Inflow to Ice Microphysics and Environmental Humidity. *Monthly Weather Review*, **123 (11)**, 3175–3193, doi:10.1175/1520-0493(1995)123⟨3175:SOSLRI⟩2.0.CO;2, URL http://journals.ametsoc.org/doi/abs/10.1175/1520-0493(1995)123⟨3175:SOSLRI⟩2.0.CO;2.

Zhang, D.-L., and K. Gao, 1989: Numerical Simulation of an Intense Squall Line during 10–11 June 1985 PRE-STORM. Part II: Rear Inflow, Surface Pressure Perturbations and Stratiform Precipitation. 2067–2094 pp.